Ocean Engineering 313 (2024) 119502

Contents lists available at ScienceDirect

Ocean Engineering

journal homepage: www.elsevier.com/locate/oceaneng

Research paper

Scour processes around pile clusters of jacket foundations under steady currents

J. Sarmiento [a], R. Guanche [a,*], I.J. Losada [a], E.M. Rosendo [b], A. Guindo [b], J. Ladrón de Guevara [b]

[a] IHCantabria, Instituto de Hidráulica Ambiental de la Universidad de Cantabria, Isabel Torres 15, 39011, Santander, Spain
[b] Dragados Offshore, Bajo de la Cabezuela S/n, 11510, Puerto Real, (Cádiz), Spain

ARTICLE INFO

Keywords:
Fixed foundation
Wind energy
Scour assessment
Offshore substation

ABSTRACT

Understanding the scour processes around offshore structures in shallow or intermediate waters is critical for ensuring their lifetime stability. Currently, there are many different formulations for simplified geometries such as monopiles, however the number of semi-empirical formulations available for complex structure types is very limited. In this context, an experimental test campaign was carried out at the IHCantabria facilities with the aim of evaluating the evolution of scour and the mechanisms that govern it on a jacket-type structure that is often used for offshore substations in offshore wind farms. The stability of this structure is ensured by pile clusters consisting of several elements, such as mud mats, pile sleeves, stiffeners and piles. Therefore, the complexity of the elements that are in direct contact with the seabed is maximal.

A series of experimental tests were carried out considering the action of the current over a sandy seabed and under live bed regime conditions ($\theta > \theta_{cr}$). The physical experiments enabled us to identify the global scour patterns around the foundation, as well as the local scour around the most exposed elements. In general, local scour developed only around the elements in contact with the seabed (i.e., pile clusters). Local scour at the most exposed pile clusters occurred in two successive phases: (1) phase 1—mud mat scour (scour around the mud mats, resulting from the blocking effect of all pile cluster elements), and (2) phase 2—local pile scour (local scour around each pile).

A dimensionless scour depth function was derived from the experiments to predict the total scour at the pile cluster contours. For this purpose, the pile cluster geometry was simplified as a vertical truncated cylinder (equivalent diameter D_{eq} and height). The dimensionless scour depth [α, β] was estimated considering only the equivalent pile cluster diameter [$S_{eq} = \alpha * D_{eq}$, where $\alpha = 0.329 - 0.389$] and taking into account a correction height factor because the pile clusters do not cover the entire water depth [$S_{eq} = \beta * D_{eq} * K_h$, $\beta = 1.1 - 1.3$]. The values obtained were consistent throughout the whole test series and are valid for predicting the total scour around similar complex-type structures (pile clusters).

1. Introduction

Over the last three decades, offshore wind energy harvesting has unlocked a significant amount of wind resources. As of the end of 2023, the cumulative capacity in Europe was 34237 MW according to (Wind Energy in Europe, 2024). Offshore wind farms have moved from near-shore sites to deep-water sites in search of better and more effective wind resources, taking advantage of economies of scale. The Vindeby Offshore Wind Farm, the first offshore wind farm built in 1991, is off the coast of the Danish Island of Lolland and has a capacity of 4.95 MW. It is located 2 km from the coast and has a maximum water depth of 4 m. However, by 2020, the average water depth and distance from the coast for offshore wind farms were 36 m and 44 km, respectively, with an average installed capacity of 788 MW ("Offshore Wind in Europe, 2020). Larger wind farms, deeper waters and greater distances from the coast usually result in harsher environmental conditions and more complex wind farm designs.

Currently, due to the average water depth of current target sites and the maturity of the supply chain, most offshore wind structures are based on bottom-fixed technologies. Monopiles are the preferred solution, but jacket and gravity-base foundations are becoming more popular. However, regardless of the technology adopted and the market situation, the structures required to harness the most desired wind

* Corresponding author.
E-mail address: raul.guanche@unican.es (R. Guanche).

https://doi.org/10.1016/j.oceaneng.2024.119502
Received 8 July 2024; Received in revised form 9 October 2024; Accepted 10 October 2024
Available online 15 October 2024

List of abbreviations and symbols

C_D –	Dimensionless drag coefficient
D_c	jacket corner column diameter
D_{eq}	equivalent pile cluster diameter
D_{pile}	pile diameter
D_{ps}	pile sleeve diamter
D_* –	dimensionless grain size
d_{50} –	sieve grain size (median)
g = 9.81 (m/s^2) –	gravitational constant
h_p	pile cluster height (up to the position of the yoke plate)
h –	water depth
K_h –	pile cluster height reduction factor
mob –	undisturbed mobility parameter (relationship between the Shields number and critical Shields number)
OSS –	Offshore Substation
R_* -	Reynolds Grain Size Number
S –	scour depth
S_{eq}	scour equilibrium depth
τ_c –	current bed shear stress
T_{char} –	characteristic time
t –	time
U_c –	mean depth-averaged current velocity
U_{rel} –	relative velocity
U_w –	Wave orbital Velocity
z_0 –	hydraulic roughness length
α –	dimensionless "total scour depth at the pile contour"
β –	dimensionless "total scour depth at the pile contour" considering the correction factor K_h
λ –	Geometric Scale factor
ρ_s –	particle density (kg/m^3)
ρ_w –	water density (kg/m^3)
θ –	Shields parameter
θ_{cr} –	critical Shields parameter
υ –	kinematic viscosity (m^2/s)
u_{*s} -	skin-friction velocity
w_s -	settling velocity

resources, which are located at greater depths, are significantly more complex than before.

Offshore substations are a crucial component of offshore wind farms because they enable the safe, efficient, and reliable transfer of electricity from offshore production facilities to the onshore grid. Their eventual failure could result in a complete blackout of the wind farm. The development of offshore substations (OSSs) is essential for ensuring the stability and efficiency of offshore energy generation. OSS engineering poses challenges in terms of design, installation, and maintenance. Most new designs consist of jacket-type structures made up of several pile clusters (), some of which have unique geometries, while others are large gravity base structures (Smulders) & (de Sonneville et al., 2014).

The presence of a structure in a fluid alters velocity patterns. When structures are found on the seabed, the interaction between the fluid and the structure modifies the velocity patterns around the foundation, generating various types of vortices that result in velocity amplification (Sumer and Fredsøe, 2002). These vortices may increase the scour potential of the fluid around the structure, triggering the development of scour holes (Whitehouse et al., 2010). In some cases, scour processes can trigger geotechnical failure or even changes in the vibration modes of the structure, which could lead to fatigue failure in the medium to long term (Den Boon et al., 2004) & (Sarmiento et al., 2021). To prevent scour, several strategies, such as those presented in () and (Raaijmakers et al., 2017), exist. These strategies have deepened into scour process mitigation, with the most commonly used being the classical rock mound designed to withstand flow amplification processes around the structure.

When studying the development of scour in non-cohesive soils, such as sands and gravels with a diameter greater than 0.063 mm, under the same current and/or wave conditions, scour is evaluated by estimating the variation in scour over time (Hoffmans and Verheij, 1997), (Sumer and Fredsøe, 2002) and (Whitehouse, 1998). This is done by determining the equilibrium scour (S_{eq}) and the characteristic time (63% of the time to reach equilibrium (de Sonneville et al., 2011)) under a steady environmental action, such as waves, currents or a combination of waves and currents. In the case of monopiles and depending on the conditions of the study, the equilibrium scour depth and characteristic time typically depend on the cylinder diameter, meteocean conditions (depth, current, and orbital wave velocity), and soil properties (d_{50} and density). Additionally, the equilibrium scour and characteristic time vary for the same structure depending on the sediment regime outside the influence of the structure (Sumer and Fredsøe, 2002) (Whitehouse, 1998).

Several semiempirical formulations for estimating scour around monopile structures due to waves, currents or a combination of both phenomena are available in the literature. Examples can be found in (Sheppard et al., 2006), (Sumer et al., 1992a), (Sumer and Fredsøe, 2002), (Sumer et al., 1992b), (Breusers et al., 1977), (Melville and Coleman, 2000), (Raaijmakers and Rudolph, 2008) or (Larsen and Fuhrman, 2023). In addition to scour processes around simple structures such as monopiles, several more complex structures such as truncated cylinders have also been investigated (Raaijmakers and Rudolph, 2008). and (Whitehouse and Stroescu, 2023) proposed new parametrizations of existing semiempirical formulations to consider the impact of a reduced pile height on the total water column during scour processes. Furthermore, several formulations have been also developed to assess the local scour around bridge piers. For instance (Evaluating Scour at Bridges, 2012), shows different approaches for different bridge piers shapes.

The number of formulations in the literature available for marine structures, more complex than monopiles, is limited. For jacket or gravity base structures, an accurate estimation of scour development is often assessed through experimental tests at reduced scale. Various examples can be found in the literature for different foundations. In the case of the classical jacket foundation composed by three or four legs (one pile per leg), some examples can be found in (Welzen et al., 2019), (Zhang et al., 2024), (Chen et al., 2023), (Chen et al., 2024), (Li et al., 2022). The scour assessment of a complex jacket foundation was also presented in (Welzel et al., 2024), while some tests related to gravity base foundations or tripod structures can be found at (Lancaster et al., 2022), (Sarmiento et al., 2024a), (Hu et al., 2021) or (Yuan et al., 2017).

However, for more complex structures, such as offshore substations (OSS), the information available in the literature is even more limited. For example (de Sonneville et al., 2014), and (Gao et al., 2023) analysed the scour process around gravity base foundations offshore substations.

Currently, offshore substations are often jacket foundations composed of several pile clusters located in the jacket corners (see Fig. 1). Above the seabed level, the pile clusters are often solid bodies extended a small percentage of the total water column and composed of several pile sleeves (from 2 to 4) connected to the jacket columns by means of vertical stiffeners and yoke plates (Fig. 1). I In addition, in many situations the mud mats are located just below the pile sleeves (Fig. 1) and act as a temporary base for the entire jacket. Below the seabed level, only the piles are extended for tens of metres. Therefore, the complex geometry of the pile clusters (several elements and different section above and below the seabed level) compared to the piles of the classical jackets composed of three or four legs with a single pile per leg

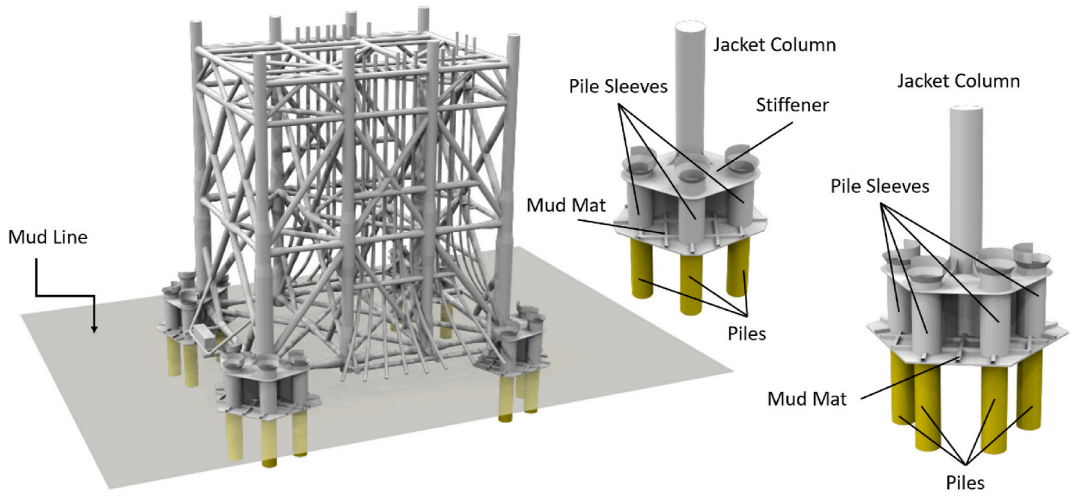

Fig. 1. Detail view of the pile clusters.

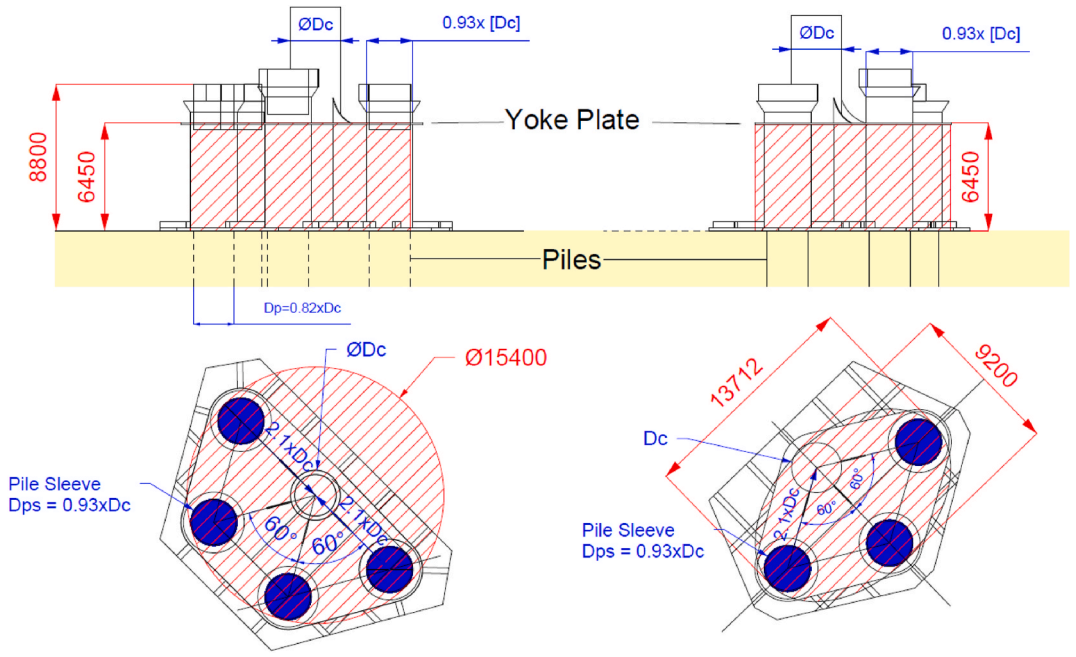

Fig. 2. Geometry of equivalent truncated piles.

(i.e. (Welzen et al., 2019), (Zhang et al., 2024), (Chen et al., 2023), (Chen et al., 2024)) limit the application of the relations proposed.

Based on this, the present study aimed to address this gap in knowledge by providing a detailed analysis of scour processes around complex jacket structures composed of several pile clusters intended for offshore wind purposes. Using a large-scale experimental test program, this study investigated scour mechanisms and estimated the equilibrium scour depth. Therefore, this paper provides a unique perspective on evaluating the importance of fluid-structure-sediment interactions on scour processes, as well as directional effects on the equilibrium scour depth. The experimental methodology used at a large-scale testing facility, specially designed for scour assessment on complex offshore structures, is also summarized.

The remainder of this paper is organized as follows. Section 1 summarizes the state of the art to prove the novelty of the present work. Section 2 introduces the target structure. Section 3 reports the experimental tests conducted and provides a brief description of the experimental facility. Section 4 analyses the results obtained and discusses the observations. Finally, Section 5 presents the conclusions of the study.

2. Case study

The case study analysed in this article is a jacket-type electrical substation with a 45 × 34.2 m footprint that is founded by 4 pile clusters (Fig. 1) at a water depth of 40 m. Two of the 4 pile clusters are each composed of 3 piles, while the remaining two are each composed of 4 piles, for a total of 14 piles. Each pile cluster includes mud mats, pile sleeves, and vertical and horizontal stiffeners, among other elements (see Fig. 1). Therefore, the geometry of the area in contact with the seabed is highly complex, and there are no available semiempirical formulations for estimating scour.

It is important to consider that as scouring occurs, the structural part in contact with the seabed undergoes changes. Under the initial conditions (zero scour), the mud mats, as shown in Fig. 1, are in direct contact with the sea bottom. As scour progresses, the mud mats become partially suspended in the water, and the piles are the only elements in contact

with the seabed. These changes in the effective geometry of the pile clusters lead to different scour mechanisms due to the modified magnitude and type of vortices generated around the jacket structure.

On the other hand, to present the results of the physical experiments in function of the dimensionless equilibrium scour depth (α and β, see next list), and taking into account the complexity of the pile clusters geometry (composed of several elements such as pile sleeves, vertical stiffeners, upper yoke plate or mud mat forming a closed substructure), the pile clusters were simplified as an equivalent truncated vertical cylinder encompassing all its elements (see Fig. 2, Table 1 and (Sarmiento et al., 2024b)). In this sense, the equivalent diameter (D_{eq}) is at least 3–5 times the diameter of the other jacket elements. Based on this, to consider that the pile groups do not extend over the entire water depth, a scour height reduction factor is considered (K_h (Raaijmakers and Rudolph, 2008)). The height of the equivalent cylinder extends from the seabed (mud mat) to the upper yoke plate (see Fig. 2). This simplification enables us to present the physical experimental results as a function of a dimensionless scour depth parameter (α and β):

- $\alpha = S_{eq}/D_{eq}$ = dimensionless equilibrium scour depth 1 (a function of the equivalent pile cluster diameter);
- $\beta = S_{eq}/(D_{eq}{}^{*}K_h)$ = dimensionless equilibrium scour depth 2 (a function of the equivalent pile cluster diameter and the height reduction factor proposed in [18]);

Where:

- S_{eq} – scour equilibrium depth (obtained from the physical experiments measurements);
- D_{eq} – Equivalent pile cluster diameter;
- $K_h = \left(\frac{hp}{h}\right)^{0.67}$ – height correction factor [18], where hp is the pile cluster height and h is the water depth.

The target site is located in the German Bright (German sector of the North Sea), where the surface layers of the seabed are composed mainly of fine sands, organic materials, and occasionally small portions of silts. For the case study, a material composed mainly of fine sands with d50 = 0.075 mm–0.12 mm (fine sands with a small percentage of silts) was considered. According to (Whitehouse, 2006), the maximum scour will always occur in granular soils (fine sands); based on this, a sandy seabed was considered to carry out the physical experiments. Table 2 summarizes the most representative characteristics of the target site: the depth, maximum annual tidal current, and bottom characteristics.

According to the seabed conditions described in Table 2, the sediment regime away from the area of influence of the structure can be considered a *live-bed regime* (θ/θ_{cr} >1). Both the Shields number and critical Shields number were estimated following the formulations described in (Soulsby, 1997).

Critical Shields Number (θ_{cr}) (Soulsby, 1997):

$$\theta_{cr} = \frac{0.3}{1 + 1.2^{*}D_{*}} + 0.055^{*}[1 - \exp(-0.02^{*}D_{*})] \quad \text{Equation 1}$$

Shields Number (θ) (Soulsby, 1997), (Shields, 1936):

$$\theta = \frac{\tau_c}{g d_{50}(\rho_s - \rho_w)} \quad \text{Equation 2}$$

Table 1
Characteristics of equivalent piles.

	Piles	Equivalent truncated cylinder		
		D1 [m]	D2 [m]	Height [m]
Mud Mat A1–A2	4	15.4	–	6.45
Mud Mat D1–D2	3	13.712	9.2	6.45

Table 2
Characteristics of the target site.

h [m]	Cu [m/s]	ρ_s [kg/m3]	d50 [mm]
40	0.43	2650	0.075–0.12

$$\tau_c = \rho_w C_D U_c{}^2 \quad \text{Equation 3}$$

$$C_D = \frac{0.4^2}{\ln\left(\frac{h}{z_0}\right)\left[\ln\left(\frac{h}{z_0}\right) - 1\right]^2} \quad \text{Equation 4}$$

According to (Sumer and Fredsøe, 2002), for a *live-bed* regime, the maximum scour depth will occur when the relative velocity (see Equation (5)) is equal to or very close to 1 (currents alone). Therefore, a set of physical experiments were designed considering the most critical conditions (i.e., currents alone) to estimate the maximum expected equilibrium scour depth.

$$U_{rel} = \frac{U_c}{U_c + U_w} \quad \text{Equation 5}$$

3. Description of the experimental tests

The experimental tests were carried out at the IHCantabria facilities, more specifically on the Cantabrian Coastal and Ocean Basin, which is classified as a Unique Scientific Facility (ICTS) by the Spanish Ministry of Science and Innovation and is managed by IHCantabria. The selected facility has dimensions of 30m × 44m with variable operating water depths between 0.2 and 3 m. The basin is equipped with a current generator. Additionally, one side of the basin is equipped with a wave generator consisting of 64 individual paddles, which include an active wave absorption system that enables the generation of waves in different directions.

The wave and current tank was divided into 5 independent sections. Two of them were filled with sand to simulate the behaviour of the granular material (i.e., sand pits or sand boxes); see Fig. 3. Based on this, two platforms were simultaneously tested combining wave free scour assessment tests and scour protection tests (the paper is only focused on the free scour assessment tests).

The dimensions of the sand boxes where the platforms were installed were 10x10 × 0.25 m. At the beginning and at the end of the platforms, two mild slopes were included to enable a smooth transition between the actual bottom of the basin and the top of the sand pits (Fig. 4). Considering the dimensions of the sand boxes, the dimensions of the platform and the capacity of the wave tank, the test scale selected to carry out the experimental tests was 1/35. The cross-sectional area occupied by the platform in each test channel was less than 1/6th of the effective cross-sectional area to avoid possible edge effects associated with the basin boundaries (Whitehouse, 1998). Each of the two sand pits was filled with fine sand with a density of 2616/m^3 and a d50 of 0.15 mm (see Fig. 5).

3.1. Scaling laws

Traditionally, all processes related to coastal and ocean engineering are studied by experimental tests on a reduced scale using Froude's similarity laws (Hughes, 1993). This approach enables a constant relation between the inertial and gravitational forces to be maintained. Occasionally, viscous effects can be relevant to some physical processes. However, viscous effects can usually be considered almost null if the Re number based on the water depth is greater than 10000; in those cases, the flow can be considered a turbulent flow (Whitehouse, 1998).

When dealing with non-cohesive materials, such as small sands or gravels, the behaviour of the seabed material will be correctly represented if the bottom, suspension and combination of both transport

Fig. 3. General view of the test tank (CCOB) and the tested platforms.

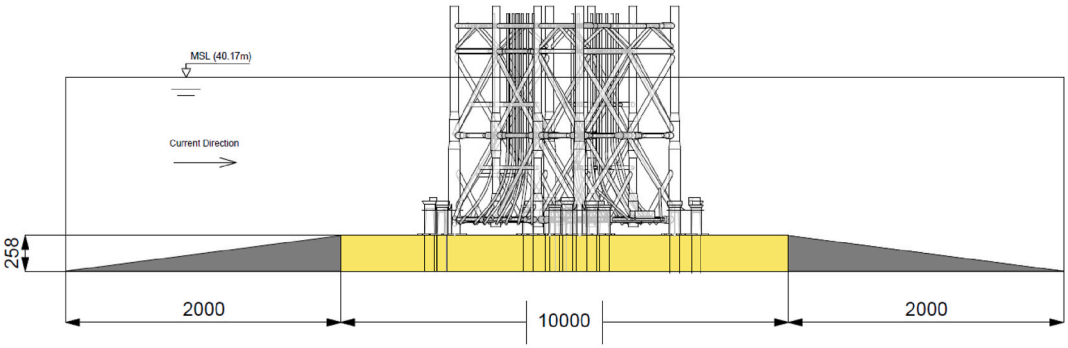

Fig. 4. Longitudinal section of the sand pits (units mm).

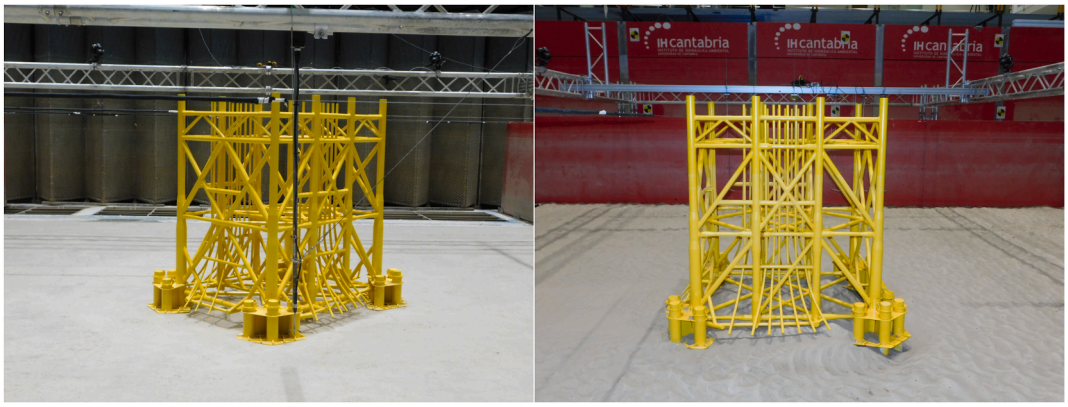

Fig. 5. General views of one of the jackets used during the experimental trials.

mechanisms are correctly represented at the laboratory scale.

In the case of sea currents, in the absence of waves, the movement of the seabed material depends on the following parameters: (1) the Shields number (θ) (Veldhuizen et al., 2023), (2) critical Shields number θ_{cr}, (3) skin-friction velocity (u_{*s}) and (4) settling velocity (w_s). Moreover, according to (Soulsby, 1997), the seabed material motion mechanism depends on the ratio between the Shields number and the critical Shields number:

- If $\theta < \theta_{cr}$ – no motion;
- If $\theta_{cr} < \theta < 0.8$ – the seabed is mobile and rippled and/or duned;
- If $\theta > 0.8$ – the seabed is mobile and flat with sheet flow;
- If $u_{*s} < w_s$ – no suspension;
- If $u_{*s} > w_s$ – the sediment is suspended.

The present case can be classified into the following seabed transport regime: $\theta_{cr} < \theta < 0.8$. Therefore, the seabed material is in a *live regime* dominated by bedload-dominated transport.

According to (Kamphuis and Herbich, 1991), when bedload transport dominates the sediment regime, sediment transport is a function of five dimensionless numbers: (1) the Reynolds grain size R_*, (2) Shields number θ, (3) relative density S_s, (4) relative length ratio $\frac{\lambda}{d}$, and (5) relative settling velocity $\frac{w}{u_*}$. Unfortunately, since the different dimensionless numbers mentioned above depend on most of the variables, perfect similarity is not possible at the laboratory scale. Therefore (Hughes, 1993), different scaling strategies are based on different dimensionless numbers: (1) the best model, which is based on the Shields number and relative density of the sediment; (2) the lightweight model, which is based on the Shields number and Reynolds grain size;

(3) the densimetric Froude model, which is based on the Shields number; and (4) the sand model, which is based on the relative density. As described in (Hughes, 1993), the scaling model that best fits bedload transport is the best model. However, the application of this model to test scales ranging from 1/30 to 1/60, which are the most common test scales, results in sediment sizes smaller than 0.063 mm. The resulting sediment is therefore a cohesive material that cannot be used for testing purposes.

An alternative model that overcomes this limitation is the light-weight model (Hughes, 1993), where both the Shields number and Reynolds grain size number remain constant at both scales. In this case, the laboratory-scale materials must have lighter densities in the model to correctly reproduce the two dimensionless numbers. In many cases, acquiring such materials is complex and usually prohibitively expensive. In addition, the difference in density between the two scales means that in many cases, the particles will enter into suspension much earlier at the model scale than at the prototype scale, and the relative fall velocity of the model will not be correctly scaled, i.e., the transport will not be correctly reproduced. Therefore, this second alternative is usually not used.

The sand model method is the simplest of all. This method simply keeps the ratio of water density to sediment density constant; hence, sediment transport is traditionally underestimated in experimental tests.

Finally, the densimetric Froude model aims only to correctly reproduce the Shields number on both scales by distorting the current velocity. However, as the critical Shields number is variable for materials smaller than $D^*<200$ (dimensionless grain size), this method will not correctly reproduce the inception of motion for fine sands.

Considering the limitations and scaling effects described above, performing experimental tests using the mobility similarity (mob) is proposed ((Veldhuizen et al., 2023)). A scaling strategy based on keeping the mobility similarity constant at the laboratory and prototype scales was developed. This means that the relationship between the Shields number and the critical Shields number (Equation (6) and Equation (7)) remains constant at both scales. By applying this scaling method, the inception of motion can be correctly reproduced during the experimental trials.

$$(mob)_{Full} = (mob)_{Lab} \quad \text{Equation 6}$$

$$\left(\frac{\theta}{\theta_{cr}}\right)_{Full} = \left(\frac{\theta}{\theta_{cr}}\right)_{Lab} \quad \text{Equation 7}$$

In Equation (6) and Equation (7), the only unknown is the current velocity at the laboratory scale. Both the characteristics at the prototype scale and the material that simulates the moving bed during the experimental tests were selected beforehand based on existing materials on the market.

Taking into account the characteristics described in Table 2 and solving Equation (7), the current velocity at the laboratory scale can be obtained (see Table 3).

Regarding the target mock-up, the platform geometry was scaled by dividing all platform dimensions by the selected geometric scale (35). The jacket tubes were reproduced using steel tubes of commercial diameters. The errors obtained between the laboratory model and the target values were always less than 5% (Figs. 3–4).

Table 3
Mobility similarity.

Full Scale			Laboratory Scale (1/35)		
C_u (m/s)	Mob (−)	h (m)	C_u (m/s)	Mob (−)	h (m)
0.43	1.25	40.17	0.34	1.25	1.14

3.2. Instrumentation, test methodology and setup

Several instruments were used to measure scour evolution and simulate meteocean conditions in the tank test.

Prior to installing the platforms in the wave-current tank, the target current was calibrated in the absence of the structures. For this purpose, 4 acoustic Doppler velocimeters (ADVs) were installed. The first was placed 2 m in front of the theoretical position of the structure and in the centre of the channel. The other three sensors were located at the theoretical position of the platform. The first sensor was at the geometric centre of the platform, the second was 1 m to the right of the first sensor, and the third was 1 m to the left of the first sensor. Once the current calibration phase was completed, the three sensors located at the theoretical position of the platform were removed, and only the sensor located 2 m in front of the structure was retained.

Scour evolution was measured using a Leika RTC360 laser scanner (Geosystems). The laser scanner measurements enabled us to check the scour evolution around the pile groups, as well as the scour measurements around the piles. All the laser scanner results presented in this paper show the difference between the initial and final scans for each time interval. The blue and green colours indicate areas of material accretion, while the yellow and red colours indicate areas of erosion.

To ensure the accurate estimation of the equilibrium scour, the current tests were divided into several steps, which enabled the measurement of the evolution of the scour over time. At the end of the test sequence, the equilibrium scour was estimated using Equation (8) ($Sd(t)$ – scour depth at time t, S_{eq} – Equilibrium scour depth, and T_{char}-characteristics time).

$$Sd(t) = S_{eq}\left(1 - e^{-\frac{t}{T_{char}}}\right) \quad \text{Equation 8}$$

The test methodology followed is briefly described in the following list: (1) scanning around the structure, (2) slowly filling the tank to the target level, (3) testing the current (for a variable time depending on the step size selected), and (4) emptying the tank (after which we return to (1)).

Two orientations were tested (Fig. 6), and the selected time steps for each are shown in Tables 4 and 5. The total effective current time (excluding the filling, emptying and laser scanner measurement times) at the laboratory scale was 30 h for direction 1 (the jacket major axis orientation parallel to the current direction) and 14 h for direction 2 (the current direction at 45° to the jacket axes). All tests were performed using unidirectional currents.

Finally, for each orientation, Fig. 6 shows the nomenclature used for the different pile clusters, piles and profiles obtained by the laser scanner.

4. Results and discussion

The results obtained are presented independently for the two jacket orientations. For each direction, the results analysed are summarized as follows: (1) global flow patterns around the structure, (2) individual scour around each mud mat, and (3) equilibrium scour estimation. The results are presented at protorype scale.

4.1. Orientation #1: Unidirectional current aligned with the major axis of the jacket

For the first orientation, physical experiments were carried out considering unidirectional currents under live bed conditions ($\theta > \theta_{cr}$). The current direction was aligned with the main jacket side. Fig. 7 shows the erosion and accretion patterns around the entire structure after the first and last time steps. Based on the laser scanners shown in Fig. 7, local scour is developed mainly in those elements that are in contact with the

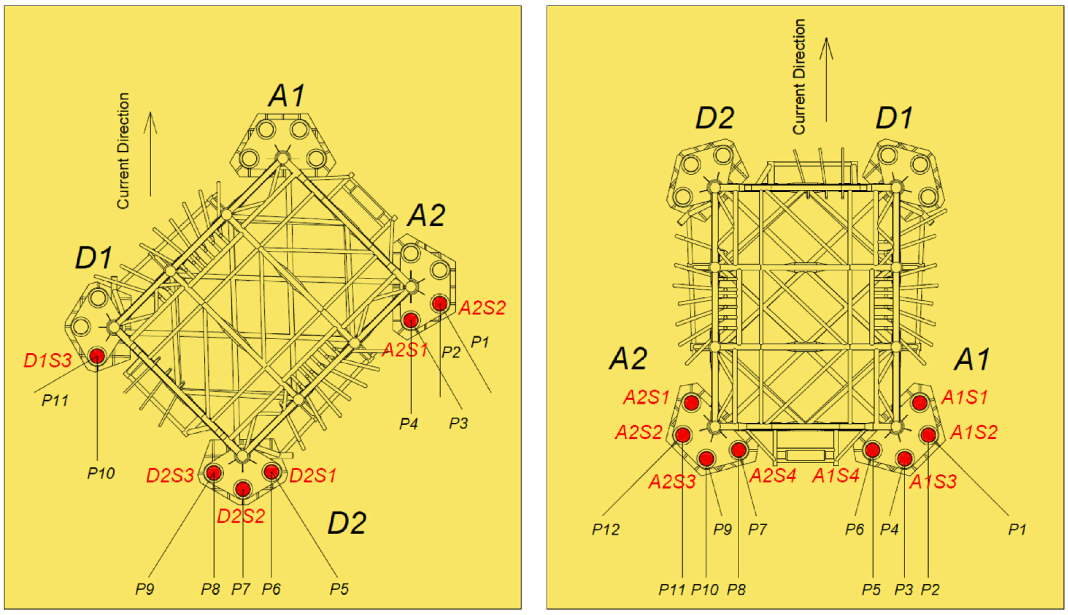

Fig. 6. Nomenclature for the pile clusters, piles and profiles.

Table 4
Orientation #1 (parallel to the jacket's major axis).

Orientation #1						
Step	Direction [degrees]	Laboratory Characteristics				
		Ind. Time [hr]	Cum. Time [hr]	h (m)	C_u (m/s)	Mob (−)
1	0	1	1	1.14	0.34	1.25
2	0	1	2	1.14	0.34	1.25
3	0	1	3	1.14	0.34	1.25
4	0	2	5	1.14	0.34	1.25
5	0	2	7	1.14	0.34	1.25
6	0	3	10	1.14	0.34	1.25
7	0	4	14	1.14	0.34	1.25
8	0	4	18	1.14	0.34	1.25
9	0	4	22	1.14	0.34	1.25
10	0	8	30	1.14	0.34	1.25

Table 5
Orientation #2 (perpendicular to the jacket's major axis).

Orientation #2						
Step	Direction [degrees]	Laboratory Characteristics				
		Ind. Time [hr]	Cum. Time [hr]	h (m)	C_u (m/s)	Mob (−)
1	45	1	1	1.14	0.34	1.25
2	45	1	2	1.14	0.34	1.25
3	45	1	3	1.14	0.34	1.25
4	45	2	5	1.14	0.34	1.25
5	45	2	7	1.14	0.34	1.25
6	45	3	10	1.14	0.34	1.25
7	45	4	14	1.14	0.34	1.25

seabed (pile clusters). Other jacket elements, such as J-tubes and vertical and horizontal bracings (located a few metres above the seabed), provide a global blocking effect, modifying the flow patterns around the foundation without inducing local scour in their vicinity.

Regarding the pile cluster configuration, Groups A1 and A2 (each consisting of 4 piles) were placed in the front part of the foundation directly exposed to the current, while pile clusters D1 and D2 were placed behind them (rear areas). Therefore, the front pile clusters A1 and A2 were eroded from the beginning of the sequence, while the erosion patterns of the rear pile clusters D1 and D2 were almost negligible. Fig. 7 shows that the seabed was undisturbed behind mud mats D1 and D2 at the end of the sequence, even though there were some areas without ripple formation.

In general, the scour mechanism around pile clusters A1 and A2 was governed mainly by the formation of a frontal horseshoe vortex and the contraction of the streamlines at the mud mat contours. The horseshoe vortex was the main factor that induced the development of scour in the front areas of pile clusters, while the contraction of the streamlines at the mud mat contours generated relevant erosion wakes behind them. The eroded material from pile clusters A1 and A2 was deposited behind them and at the inner location of the jacket footprint. For both front pile clusters (A1-A2), Figs. 8 and 9 show the scour evolution for time steps 1–3–5–7–8–10.

It is to be noted that, the development of global scour around the entire footprint of the jacket foundation was not observed during the physical experiments. Additional time could allow the propagation of erosion wakes from the front to the rear pile clusters (i.e., the outer and inner wakes). However, considering the current velocity, the location of the material eroded from the front pile clusters (mainly deposited at the inner jacket locations) and the orientation of the foundation relative to the current position, the time required to allow the development of global scour would appear to have been too long.

Having described the general scour patterns above, the next sections focus mainly on identifying the scour mechanism and the equilibrium scour depth around the most exposed pile clusters (A1–A2, front pile clusters).

4.1.1. Scour mechanism around the most exposed pile clusters (A1 and A2)

First, a good understanding of the scour mechanism is key for estimating the equilibrium scour depth. In general terms, based on the visual inspections carried out during the execution of the tests, the photo analysis and the laser scanner measurements (see Figs. 8 and 9), it was found that the scour mechanism around the most exposed piles (see Fig. 11) was developed in two successive phases:

1. Phase 1 (see Fig. 10) – Mud mat scour (due to the blocking effect of all pile cluster elements):

Initially, scour developed around the contours of the external mud mat. The scour was generated mainly by the blocking effect of all

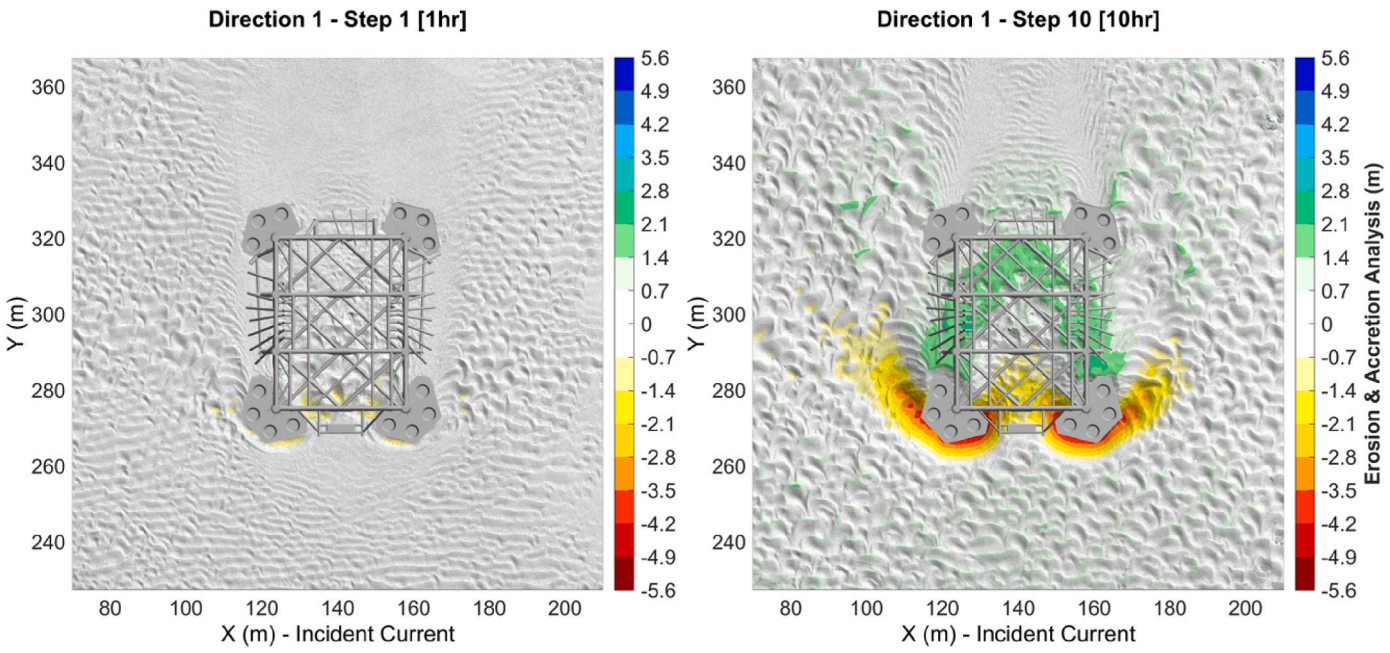

Fig. 7. Orientation 1: Laser Scanner: 1) Left: Step 1 (1 h laboratory scale); 2) Right: Step 10 (30 h laboratory scale).

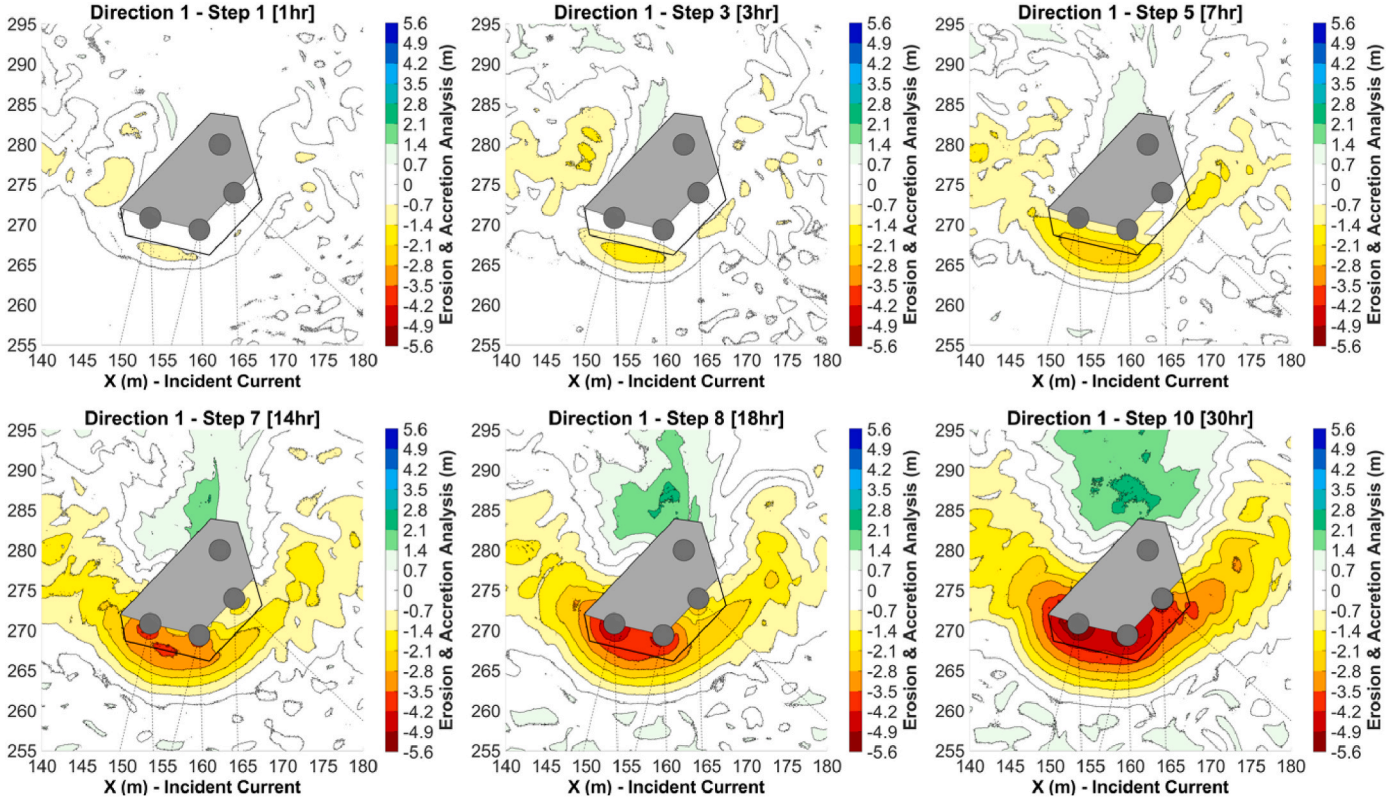

Fig. 8. Orientation 1: Erosion evolution around Pile Group A1. Top row: Steps 1–3–5. Bottom row: Steps 7–8–10.

elements of the pile cluster located above the seabed (pile sleeves, mud mat and stiffeners). The maximum scour depth occurred just outside the mud mat footprint (close to the mud mat contour, see the green circle on the left side in Fig. 10), as the scour measured at the pile contour was always lower than that measured outside the mud mat. This scour mechanism can be observed in the first row of Figs. 8 and 9, as well as in the sketch shown in Fig. 10 (left side, longitudinal profiles from the centre of the pile).

In general, the initial scour mechanism around the pile clusters and mud mats (Phase I) is mainly controlled by the downflow through the pile sleeves, the development of a frontal horseshoe vortex, the contraction of the streamlines at the mud mats lateral sides and the lee wake vortex behind the pile groups. Based on this, the flow is amplified around the pile clusters and mud mat contour increasing the bed shear

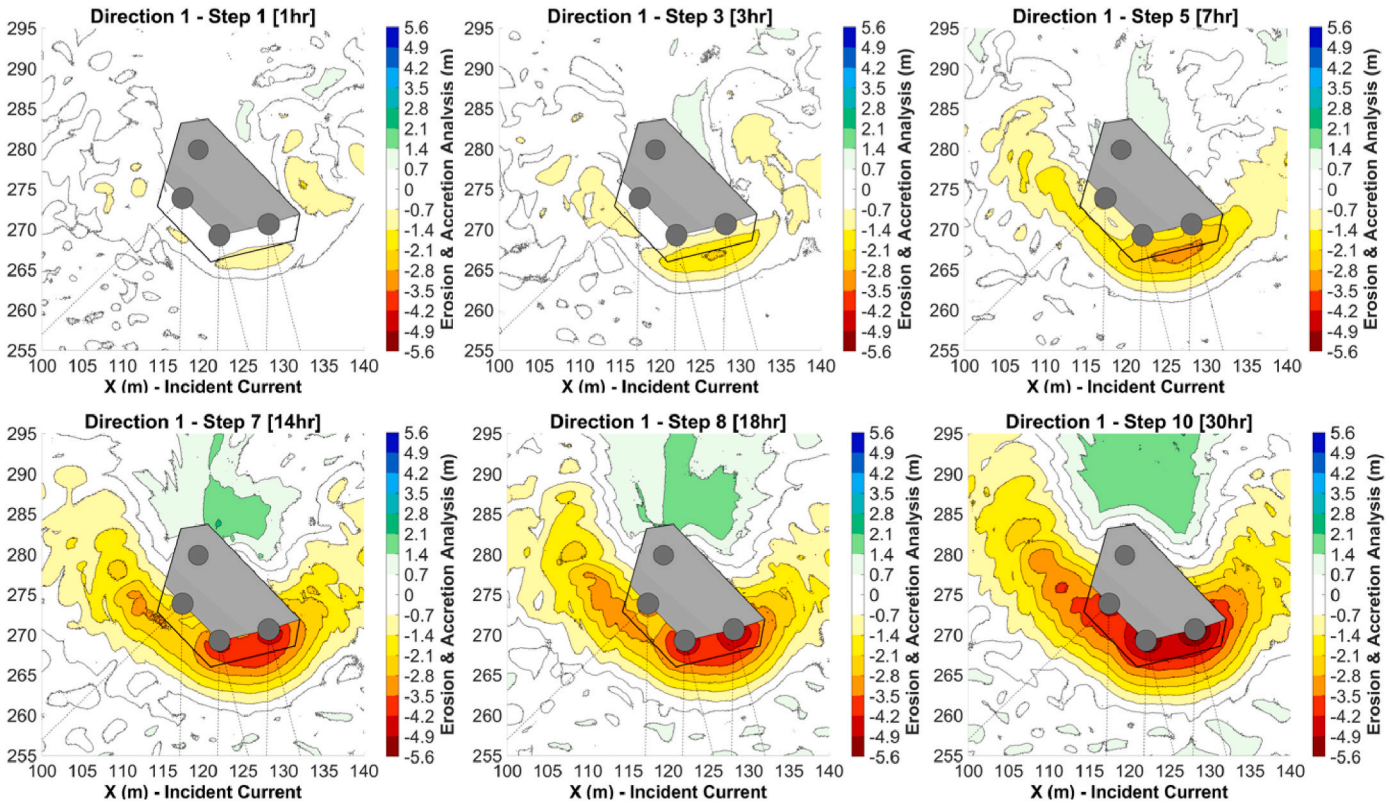

Fig. 9. Orientation1: Erosion evolution around Pile Group A2 (time intervals 1–3–5–7–8–10).

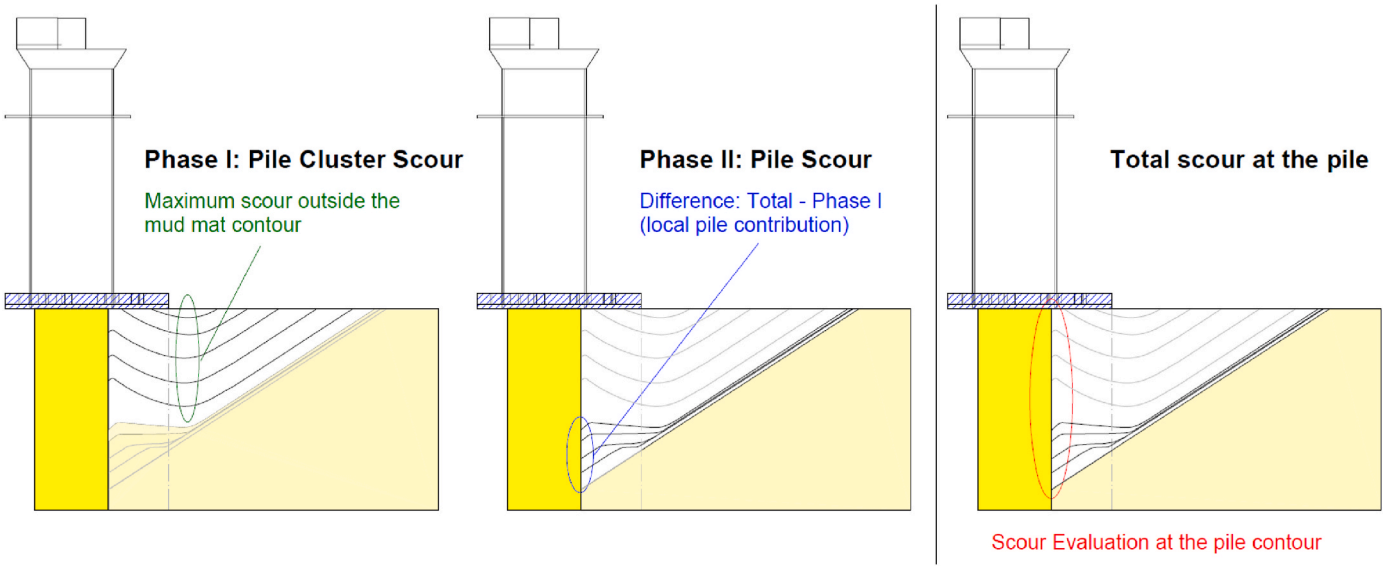

Fig. 10. Scour mechanism around the pile cluster: 1) Left: phase I – mud mat scour, 2) centre: phase II – local pile erosion, and 3) right: total scour at the pile.

stress and triggering scour processes around the mud mats.

In the case of the front part of the mud mats, based on visual inspections and laser scanner measurements, the mechanism controlling the scour around the pile clusters depends mainly on the relative angle of attack between the flow and the mud mat contour. On the mud mat side parallel to piles S3–S4 (pile clusters A1 and A2, see Fig. 11), the angle between the current direction and the mud mat side was 75° (almost perpendicular to the flow direction, Fig. 11). At this location, the scour development seems to be mainly controlled by a frontal horseshoe vortex generated as a consequence of the pile cluster and mud mat blockage effect. This phenomenon can be clearly observed in the upper laser scanner presented in Figs. 8 and 9 (steps 1, step 3 and step 5). Besides, moving to the mud mat contour parallel to piles S2 and S3, the angle of attack of the mud mat plate with respect to the flow increased to 45° (Fig. 11). Although the presence of the horseshoe vortex was also observed at this location, the development of the scour in these areas seems to have been induced by the contraction of the streamlines.

Furthermore, erosion wakes are also extended behind the inner and outer sides of the mud mats (Fig. 7, left side). The extent of the erosion wakes is longer at the outer mud mat contour (behind pile S1-S2, see

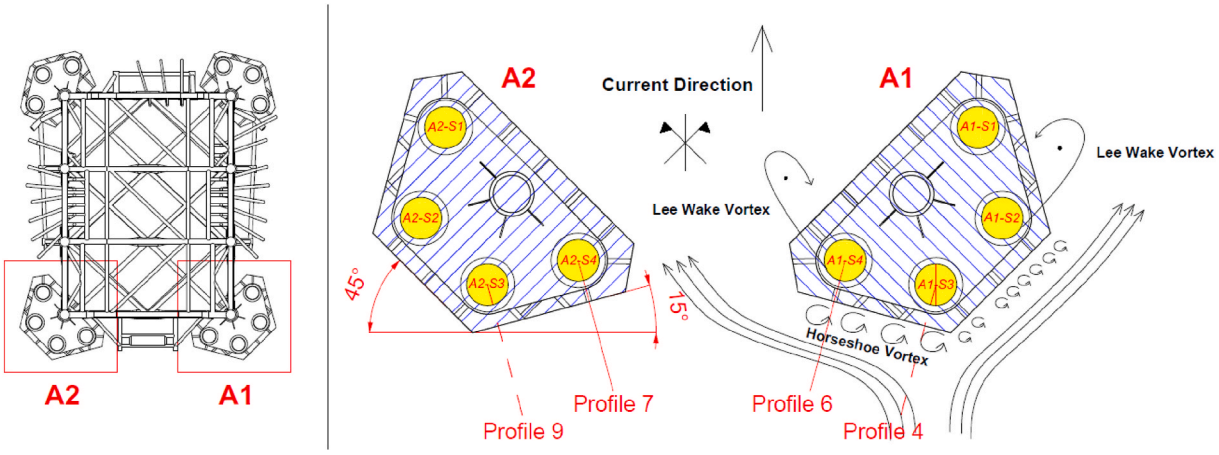

Fig. 11. Orientation 1: Pile clusters A1 and A2.

Figs. 7 and 11) in comparison to the inner sides (behind pile S4, see Figs. 7 and 11). This phenomenon occurs as a result of the global blocking effect of the jacket elements (i.e. horizontal and vertical frames), which reduces the flow at the inner jacket areas and increase the flow velocity at the external jacket contours.

During this phase, the influence of the piles on scour development may be considered negligible. The erosion at the pile contour was always lower than that at the mud mat contour (see Fig. 10, left side).

2. Phase 2 – Local pile scour:

When the scour at the edge of the mud mat and at the pile is equivalent, a local scour around each pile is be developed (see Fig. 10, blue circle). Basically, when the distance between the mud mat and the seabed is enough to allow the flow penetration, a local horseshoe vortex is generated, eroding the area located around each pile.

For the case evaluated, the distance between the centre of the piles and the side of the mud mat was approximately 3 m, and the diameter of the piles was 2.45 m. Further analysis should be carried out to analyse in detail the influence of the distance between the piles and the mud mat. For instance, in those cases where the mud mat would only be extended up to the pile sleeve contour, both phases described above would be simultaneously developed from the beginning of the test.

Comparing the scour mechanism described above with other complex foundations previously investigated, both phases described around the OSS pile clusters, mud mats and piles can be considered as "similar" to the scour process around complex bridge piers. However, significant differences can be observed since the geometry of the OSS is significantly different in comparison to the classical complex bridge piers.

In the complex bridge piers, the total scour depth can be computed as the sum of the pier stern, pile cap and pile group contribution according to (Evaluating Scour at Bridges, 2012). However, in the study case presented in this paper, the local scour around the pile clusters should be computed as the sum of the mud mat scour (phase I, mud mat, pile sleeves, stiffeners, yoke plate) plus pile scour (phase II). The contribution of the upper jacket structure (lattice) to the local scour can be considered negligible since the seabed deformation observed below the lower horizontal bracing (closer elements to the seabed and j-tubes) is negligible in comparison to the seabed deformation observed around the pile clusters.

To clarify the behaviour described above, different longitudinal profiles were estimated from the centre of the exposed piles (A1S3–A1S4–A2S3–A2S4, Figs. 6 and 11). Given the symmetry between pile clusters A1 and A2, the analysis conducted below is focused on pile cluster A2.

With regard to the evolution of the scour at the piles, for pile A2S4 (Profile 7 – Figs. 11), Fig. 12 shows the longitudinal profiles after each time step. The meaning of the set of lines in Fig. 12 is summarized as follows:

- The dashed vertical grey line shows the position of the mud mat contour.
- The solid vertical black line shows the pile contour.
- The dashed vertical grey line shows the laser scanner profiles (steps 1–9).
- The solid black line shows the last laser scanner profile (step 10).

The evolution of the longitudinal profiles in Fig. 12 clearly shows the scour phases described above. The red circle shows the evolution of scour during phase I (5–6 steps). During this phase (grey dashed lines), the maximum scour depth always occurred close to the mud mat contour, and the erosion at the pile contour was always lower than that at the mud mat contour. Later, when the erosion at the mud mat was equivalent to the erosion at the pile, local scour around the pile developed (phase II – the green circle in Fig. 12). An equivalent behaviour was observed for piles A1S4–A1S3–A2S3. For piles A1S2 and A2S2, the scour mechanism observed was equivalent to that observed for the most exposed piles, although the magnitude of erosion was delayed over time. Additional time would have been required to ensure that the equilibrium conditions were reached (the maximum expected scour depth should have been equivalent to the magnitude observed at the S3 and S4 piles). Piles A1S1 and A2S1 are located in the shaded area; therefore, the scour observed at the end of the sequence was lower.

On the other hand, very similar erosion patterns can be observed in the inner areas of the mud mats between the piles. For example, Fig. 13 shows the longitudinal profile obtained between piles A2S3–A2S4. In Fig. 13:

- The dashed grey lines show the longitudinal profiles after each time step.
- The black solid line shows the longitudinal profile after the last scan.
- The vertical grey solid line represents the intersection between the longitudinal profile and the mud mat contour.
- The vertical solid dashed line shows the intersection between the longitudinal profile and the theoretical line connecting the centres of piles A2S3–A2S4.

Figs. 13 and 12 show that, initially, the maximum erosion occurred on the outer contour of the mud mat in phase I (first 5–6 intervals). However, from intervals 5–6, the maximum scour moved through the areas below the mud mat footprint. In the last scan, the maximum scour was located at the theoretical intersection between the longitudinal

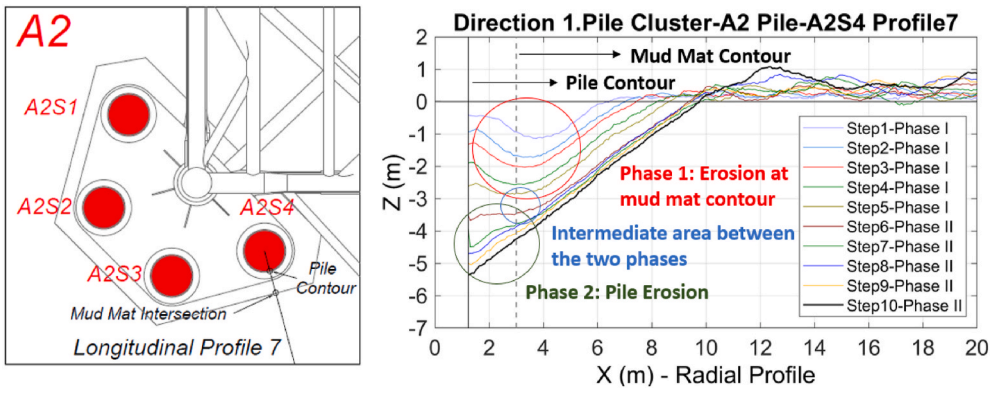

Fig. 12. Orientation 1: A2S4 longitudinal profiles: Profile 7.

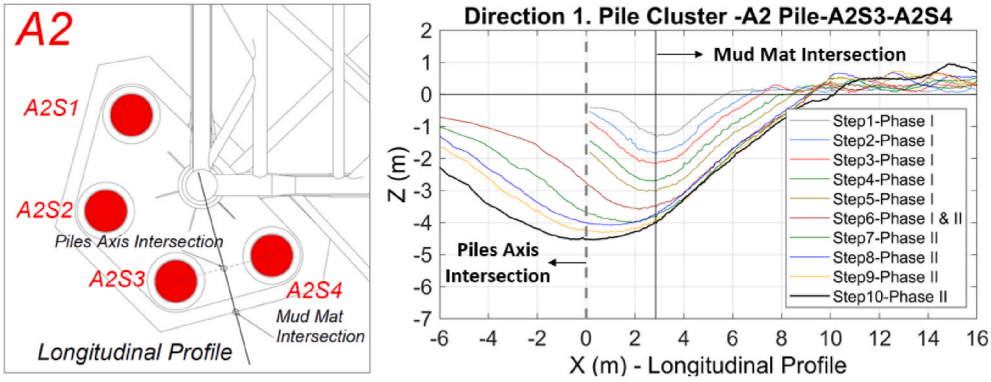

Fig. 13. Orientation 1: Longitudinal profile between piles A2S4-A2S3.

profile and the theoretical straight line connecting the centres of piles A2S3–A2S4 (dashed grey line). The maximum scour in these areas was approximately 4.5 m, which is 1 m lower than the maximum scour depth measured at the piles contour (A2S3–A2S4).

Furthermore, comparing the longitudinal profiles from the pile A2S4 (Fig. 12) and the longitudinal profile located between both piles (Fig. 13), as well as the erosion maps presented in Figs. 8 and 9 (mainly from step 7–8 to the end), it can be observed how the maximum local scour was reached at the contour of the piles (~5.4–5.99m) being the erosion measured between them smaller (~4.5m, Fig. 13). This reduction on the erosion magnitude in the area located between both piles respect to the maximum local scour reached at the pile contour is aligned with previous experiences presented in (Sumer and Fredsøe, 2002) for pile groups or in the experimental results presented at (Yang et al., 2020) to assess the scour development around different pile groups configurations.

4.1.2. Equilibrium scour depth at the most exposed pile clusters (A1 and A2)

The total equilibrium scour depth was estimated at the contour of the most exposed piles (Fig. 10, right side), where the final equilibrium condition was reached at the end of the sequence (piles A1S3–A1S4 and A2S3–A2S4). In addition, to characterize the scour evolution described above, the equilibrium conditions were also assessed for the two phases described.

The following list summarizes the equilibrium conditions used to characterize scour development around the pile clusters:

1. Total scour depth at the pile contour: the scour measured at the contour of the pile according to the sketch presented in Fig. 10; on the right-hand side, the data from all time steps were used.
2. Estimation of the equilibrium scour depth for the different phases described above.
   2.1 Phase I (Fig. 10, left side): the scour equilibrium depth at the mud mat contour. Only the data corresponding to phase I are used to estimate the equilibrium conditions (5–6 steps).
   2.2 Phase II (Fig. 10, centre side): the local pile scour. This condition was estimated as the difference between the total scour depth at the pile cluster contour and that of phase I ($S_{eq-Phase\ II} = S_{eq} - S_{eq-Phase\ I}$).

For all conditions, the selected experimental data were fitted to Equation (8) to estimate the equilibrium condition (S_{eq}).

Once the equilibrium condition was estimated, the dimensionless scour depth ($\alpha = S/D$) was also estimated for the three conditions described above:

$$S_{eq} = \alpha^{*} D_{eq} \quad \text{Equation 9}$$

$$S_{eq-Phase\ I} = \alpha_{Phase\ I}{}^{*} D_{eq} \quad \text{Equation 10}$$

$$S_{eq-Phase\ II} = \alpha_{Phase\ II}{}^{*} D_{pile} \quad \text{Equation 11}$$

Where:

- S_{eq} = total scour depth at the pile contour;
- $S_{eq-Phase\ I}$ = equilibrium scour depth at the mud mat contour (phase I);
- $S_{eq-Phase\ II}$ = local equilibrium scour depth at the piles (phase II, without considering the contribution of phase I);
- α = dimensionless "total scour depth at the pile contour";
- $\alpha_{Phase\ I}$ = dimensionless "scour depth at phase I (mud mat contour)";

- $\alpha_{Phase\ II}$ = dimensionless "scour depth at phase II (local scour around the piles without considering the phase I scour)";
- D_{eq} = equivalent pile cluster diameter (see Table 1);
- D_{Pile} = pile diameter (2.45 m).

In addition, as noted in Section 2, the dimensionless scour depth (β) was also estimated considering the truncated height of the pile clusters:

$$S_{eq} = \beta^{*}D_{eq}{}^{*}K_h \quad \text{Equation 12}$$

$$S_{eq-Phase\ I} = \beta_{Phase\ I}{}^{*}D_{eq}{}^{*}K_h \quad \text{Equation 13}$$

Where:

- β = dimensionless "total scour depth at the pile contour" considering the corrector factor K_h;
- $\beta_{Phase\ I}$ = dimensionless "scour depth at phase I (mud mat contour)", considering the correction factor K_h.

4.1.2.1. Total equilibrium scour depth at the pile contour. For the most exposed piles (A1S4–A1S3 and A2S4–A2S3, Fig. 11), the final equilibrium scour depth (Table 6) was estimated by fitting Equation (8) to the experimental data measured at the pile contour (Fig. 10, right-side, for the first step scour at the pile contour, could not be measured). Fig. 14 shows the scour evolution over time for piles A2S3 and A2S4.

According to the results, as shown in Table 6, the equilibrium condition varied from 5.4 to 5.99 m; the dimensionless scour depth (1), $\boldsymbol{\alpha}$, varied from 0.35 to 0.389; and the dimensionless scour depth $\boldsymbol{\beta}$ (2, considering the relative height of the pile cluster) varied from 1.17 to 1.3. Notably, the dimensionless scour depth was similar to the value proposed by (Sumer and Fredsøe, 2002) for slender elements.

Considering the pile cluster set-up, the erosion observed at the rear piles of piles in clusters A1 and A2 did not reach equilibrium at the end of the tests. It is expected that with increasing duration of the test, the erosion reached at piles A1S1, A1S2, A2S1 and A2S2 would have been equivalent to the magnitude observed at the front piles.

4.1.2.2. Intermediate phase equilibrium scour depth (phase I mud mat edge). Once the total near-pile scour depth was assessed and estimated, the equilibrium scour depth and the dimensionless scour depth were assessed individually, taking into account the two scour phases described above. As in the case of the "total equilibrium scour depth at the pile contour", the equilibrium condition was assessed only for the most exposed piles.

For phase 1 (mud mat scour depth), the equilibrium condition was assessed just in front of piles A1S4–A1S3 and piles A2S4–A2S3 (the most exposed areas; see Figs. 8, 9 and 11).

According to the longitudinal profiles shown in Fig. 12 (profile 7 A2S4), phase I clearly developed during the first 5 steps of the test sequence. Under these conditions (from step 1 to steps 5–6), the maximum scour depth was measured outside the mud mat footprint (according to the maximum scour values shown in Fig. 10 on the left).

Table 6
Orientation 1: Equilibrium scour depth and dimensionless equilibrium scour depth at the most exposed piles (total).

Equilibrium Condition: Total Scour Depth at the Pile Contour			
Pile	Equilibrium Scour Depth (S_{eq})	Dimensionless Scour Depth (1) $\boldsymbol{\alpha = S_{eq}/D_{eq}}$	Dimensionless Scour Depth (2) $\boldsymbol{\beta = S_{eq}/(D_{eq}xK_h)}$
A1S3	5.67	0.368	1.23
A1S4	5.99	0.389	1.3
A2S4	5.87	0.381	1.27
A2S3	5.4	0.35	1.17

D_{eq} = 15.4 m (equivalent pile diameter)//K_h = 0.299.

Fig. 15 shows the evolution of scour at the mud mat contour just in front of piles A2S4 (left plot) and A2S3 (right plot) considering steps 1–5 (symmetrical values were obtained at pile cluster A2).

Finally, the equilibrium scour depth after phase 1 (the mud mat contour, see Fig. 10) is presented in Table 7. As in previous cases, Table 7 includes the estimated equilibrium scour depth as well as the dimensionless scour depth parameters with ($\boldsymbol{\beta}$) and without ($\boldsymbol{\alpha}$) considering the relative height of the pile cluster with respect to the total water depth. According to the results presented in Tables 7 and in the most eroded areas, the mud mat equilibrium scour depth was approximately 3 m.

Finally, considering the results presented above with respect to the total equilibrium scour depth, as well as the equilibrium scour depth obtained at the mud mat contour at the end of phase I, the local scour around the most exposed piles (phase II, Fig. 10) was evaluated, taking into account the difference between the total equilibrium scour depth and the phase I equilibrium scour depth. Table 8 shows the equilibrium scour reached at phase II (the magnitude of the scour and the dimensionless scour depth $\boldsymbol{\alpha}$):

Table 8 shows that the equilibrium scour during phase 2 (local scour around the piles) varies between 1.00 and 1.18 times the pile diameter. The equilibrium scour depth proposed for slender individual cylinders at (Sumer and Fredsøe, 2002) is 1.3 times the pile diameter. Therefore, the dimensionless scour depth obtained during the phase II is slightly smaller than the classical value proposed for a single slender vertical cylinder (Sumer and Fredsøe, 2002).

4.2. Orientation #2: Direction of flow at 45° to the jacket axes

As in the previous case, this test was also carried out under live bed conditions ($\theta > \theta_{cr}$). Fig. 16 shows the laser scanner measurements around the entire foundation after the first and last time steps. Both laser scanner measurements show the global erosion pattern around the foundation. In this second configuration, pile clusters A2, D2 and D1 were directly exposed to the currents (Fig. 16). Lee wakes behind these pile clusters protruded a few metres behind them. On the other hand, there was a stagnation point just behind mud mat D2 (inside the jacket) where sediment accumulated. By analysing Fig. 16 in detail, we can see that this entire shaded area was projected behind the foundation, avoiding the development of scour in pile cluster A1. In fact, the seabed located behind pile cluster A1 was flat and undisturbed, without even ripple formation.

Fig. 17 (pile cluster D2), Fig. 18 (pile cluster A1) and Fig. 19 (pile cluster D1) show detailed laser scanner views of the local scour around the most exposed pile clusters. The evolution of the scour after each time step can be seen in these figures. The scour mechanism identified is consistent with the description presented above (orientation 1).

Next, the evolution of the scour around the exposed pile clusters was widely examined (D2, D1 and A2). The scour mechanism was identified, and the scour was evaluated over time.

Considering the different orientations of the pile clusters for this orientation, the results were classified individually by pile cluster. For each pile cluster (D2, A2 and D1), the scour mechanism and the equilibrium scour depth are presented below. In general terms, the scour mechanism observed in direction 2 around the pile clusters are aligned with the scour mechanism described in orientation 1.

4.2.1. Pile Cluster D2

With regard to pile cluster D2 (the front pile cluster), Fig. 17 shows in detail the development of the scour after each time step (steps 2–3–4–5–6–7). Initially, the scour in front of pile cluster D2 (see Fig. 20) was generated mainly by the development of a horseshoe vortex along the entire front contour of the pile cluster combined with the contraction of the streamlines on either side of the central pile (D2S1) and the lee wake vortex behind. The erosion patterns measured on the contour of mud mat D2 (Fig. 17) showed symmetrical behaviour, although the erosion measured around pile D2S3 was slightly greater (left side of

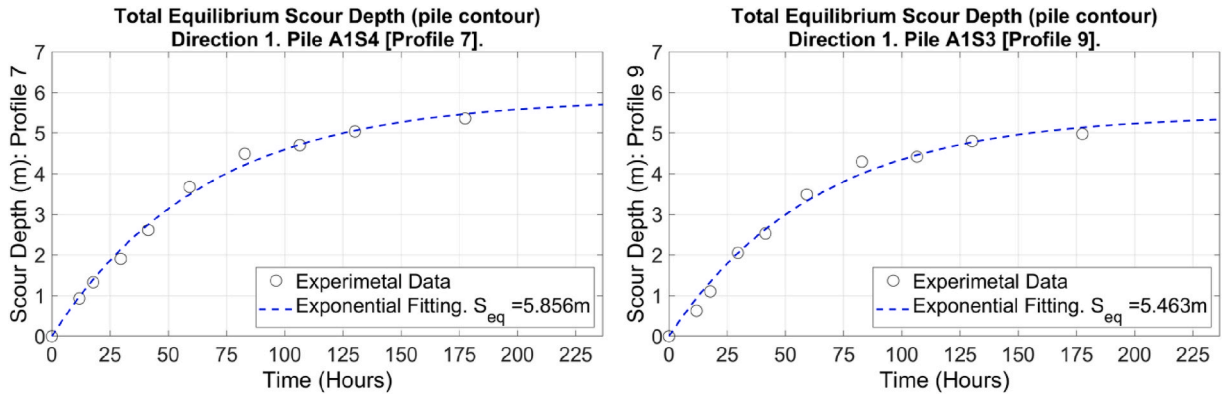

Fig. 14. Orientation 1: Total equilibrium scour depth at the pile contour: (1) Left: pile A2S4 and (2) right: pile A2S3.

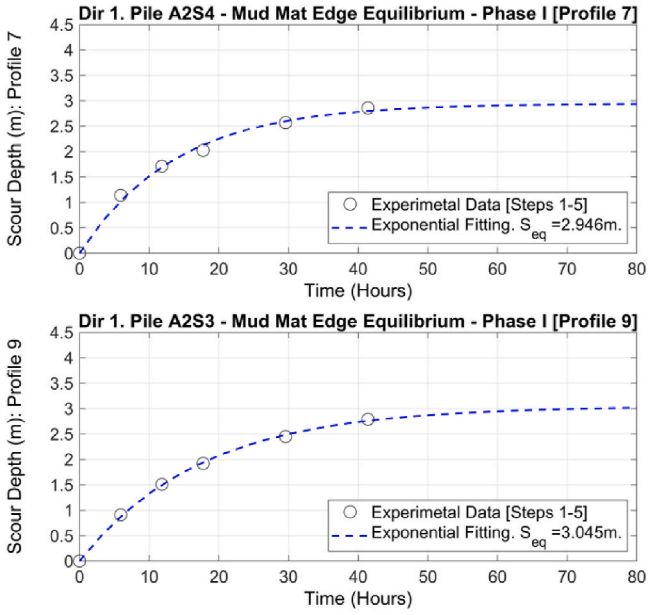

Fig. 15. Orientation #1: Equilibrium scour at the mud mat contact in front of piles A2S4 (left) and A2S3 (right).

Fig. 17). In general, this scour mechanism was quite similar to that of phase I (mud mat scour), which is described for the first orientation around pile clusters A1 and A2.

Analogous to orientation #1, Fig. 21 (D2S2) and Fig. 22 (D2S1 and D2S3) show the longitudinal profiles from the centres of the piles and perpendicular to the mud mat contour. In these figures (Figs. 21 and 22), the dashed vertical line (close to 3 m) shows the mud mat contour, while the solid vertical line shows the pile contour. The grey lines show the longitudinal profiles at the end of each time interval, while the black line shows the final profile obtained after the last scan (see Fig. 23).

For the outer piles (D2S1 and D2S3, Fig. 20), the longitudinal profiles shown in Fig. 22 show that at the end of the test sequence, local scour at the pile (phase II) had not developed. On both sides (D2S1 and D2S3), the erosion at the pile contour was always lower than that at the mud mat contour (red circles Fig. 22).

On the other hand, the behaviour observed in pile D2S2 (central) is also consistent with the behaviour observed in the outer piles. Due to the configuration of the pile cluster, the erosion measured in the first steps was slightly lower than that observed in piles D2S1 and D2S3, possibly due to the presence of a stagnation point. Fig. 21 depicts, between the two last time steps, where the erosion on the mat contour was equal to the erosion at the pile contour. From this step, the local erosion at the contour of the pile D2S2 began (phase 2), following the same mechanism described for pile groups A1 and A2 of orientation #1.

As phase II did not develop, the equilibrium scour depth was only estimated for phase I (the maximum erosion at the mud mat contour, Fig. 10, left side). The main results, including the equilibrium scour depth and dimensionless scour depth (α and β), are presented in Table 9.

Regarding the equilibrium scour at the mud mat contour (phase I), the dimensionless parameters α and β estimated for both orientations were similar. For the most exposed piles of pile cluster D2 for orientation #2, the obtained values were [$\alpha = 0.18$–20 and $\beta = 0.58$–0.65], while for the most exposed piles of pile clusters A1 and A2 for orientation #1, the obtained values were [$\alpha = 0.19$–20 and $\beta = 0.64$–0.67].

4.2.2. Pile Cluster A2

For pile cluster A2, the erosion evolution at the end of each time step (2–3–4–5–6–7) is shown in Fig. 18. In general, the scour was located mainly in the front piles (A2S1 and A2S2, Fig. 24). Fig. 18 also shows the progression of erosion under the mud mat.

The scour in the front piles (A2S1 and A2S2) developed mainly by the combination of a horseshoe vortex, the contraction of the flow lines at the mud mat contours, and the generation of lee wake vortex behind the pile cluster (see Fig. 24, left side). The relative angle between the contour of the mud mat (parallel to piles A2S1–A2S2) and the flow direction (i.e., 45°) reduced the influence of the horseshoe vortex and increased the potential scour induced by the contraction of the streamlines, triggering the development of an erosion wake behind the pile cluster.

For the most eroded pile (A2S2, see Figs. 24), Fig. 25 shows the longitudinal profiles from the centre of the pile. At the contour of pile A2S2, the total estimated equilibrium scour depth was 5.06 m. Considering an equivalent pile diameter of 15.4, the dimensionless α and β parameters were $\alpha = 0.329$ and $\beta = 1.1$, respectively.

4.2.3. Pile Cluster D1

Finally, Fig. 19 shows the evolution of scour around pile group D1. In this case, the scour developed mainly around pile D1S3 (the front pile). Two erosion wakes were observed on either side of pile D1S3 (see Fig. 19). The scour observed at the rear piles was much less than that at pile D1S3.

For the most eroded pile (D1S3, see Figs. 24), Fig. 26 shows the longitudinal profiles from the centre of the pile (during the first two steps, the scour measured at the pile contour was too small and could not be measured). Moreover, due to the pile cluster orientation, the scour observed at the mud mat contour was smaller than that at other orientations.

The total equilibrium scour depth at pile D1S3 was approximately 3.5 m. According to Fig. 2, assuming an equivalent pile diameter of $D_{eq} = 9.2$ m), the estimated dimensionless parameters α and β were $\alpha = 0.38$ and $\beta = 1.27$, respectively. The dimensionless scour depth values were in

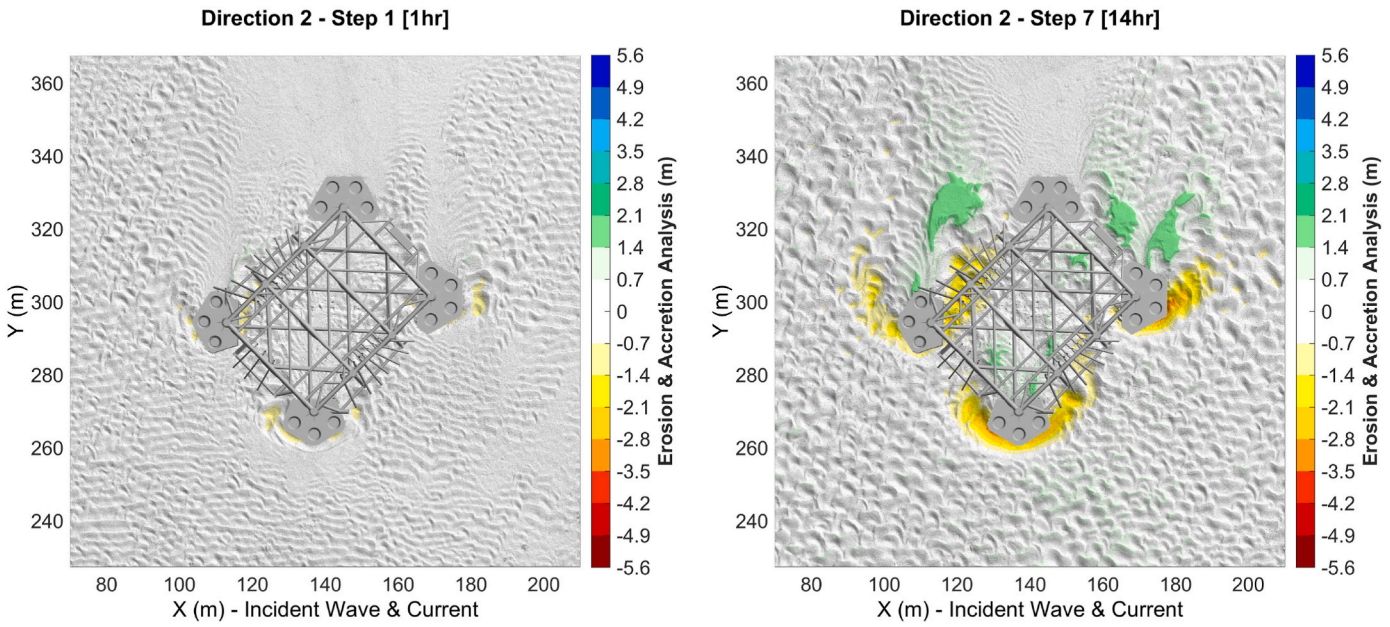

Fig. 16. Orientation #2: (1) Left: laser scanners after the first step and (2) right: last scan.

Table 7
Orientation #1: Equilibrium scour depth and dimensionless equilibrium scour depth considering only the scour at phase I (the mud mat contour).

Equilibrium Condition: Phase I			
Pile	Equilibrium Scour Depth (S_{eq})	Dimensionless Scour Depth (1) $\boldsymbol{\alpha = S_{eq}/D_{eq}}$	Dimensionless Scour Depth (2) $\boldsymbol{\beta = S_{eq}/(D_{eq}xK_h)}$
A1S3	3.08	0.2	0.67
A1S4	3.1	0.201	0.65
A2S4	3.04	0.197	0.66
A2S3	2.95	0.192	0.64

D_{eq} = 15.4 m (equivalent pile diameter)//K_h = 0.299.

Table 8
Orientation 1: Final equilibrium scour: A1S3, A1S4, A2S3 and A2S4.

Equilibrium Condition: Phase II		
Pile	$\boldsymbol{S_{eq}}$– Phase II [m]	Dimensionless Scour Depth $\boldsymbol{\alpha = S_{eq-PhaseII}/D_{Pile}}$
A1S3	2.59	1.05
A1S4	2.89	1.18
A2S4	2.83	1.16
A2S3	2.45	1.00
D_{pile} = 2.45 m		

line with the values obtained from previous results corresponding to pile clusters A1 and A2 of orientation #1.

5. Summary & conclusions

At present, there are no semiempirical "ad hoc" formulations for estimating the equilibrium scour of complex bottom-fixed structures such as jackets composed of several pile clusters. On this basis, physical experiments were carried out to investigate the scour processes around a complex jacket structure, particularly around the pile clusters widely used to ensure its stability.

A series of physical experiments were performed under a live bed regime, which, combined with a high-resolution laser scanner, enabled us to identify the scour processes, as well as the scour equilibrium depth at the most exposed piles.

From a general perspective of the scour processes, the following conclusions were obtained:

- The global erosion patterns around the whole structure was identified. A significant amount of the material eroded from the pile clusters was deposited at the inner areas of the jacket foundation.
- Local scour around individual elements of the jacket were observed only around elements in contact with the seabed (pile clusters).
- In general, the erosion around each pile cluster developed in two clearly differentiated phases:
  - *Phase 1 - Mud mat scour:* Initially, scour developed around the external mud mat contour due to the blocking effect of all elements of the pile cluster located above the seabed. The maximum scour depth occurred just outside the mud mat footprint.
  - *Phase 2: Local scour at each of the piles*: When the scour at the edge of the mud mat and at the pile was almost equal, local scour around each pile was triggered.

With regards the importance of flow orientation, the following conclusions were achieved:

- *Flow parallel to the major jacket axes:* The maximum scour was developed in pile clusters A1 and A2. Next, the scour process main outcomes will be synthetized based on the two steps process identified.
  - o Total Scour at the pile contour: The total equilibrium scour depth at the pile contour was S_d = [5.4–5.99 m], while the observed dimensionless scour depth was α = [0.35–0.389]. Finally, the observed dimensionless scour depth, as a function of the equivalent diameter and the relative height of the pile cluster, was β = [1.17–1.3].
  - o Phase 1: Mud mat scour: The mud mat contour equilibrium contour depth was S = 2.95–3.1 m; while the dimensionless scour depth (a function of the equivalent pile cluster diameter) was $\alpha_{Phase\ I}$ = [0.192–0.2]. Finally, the observed dimensionless scour depth was $\beta_{Phase\ I}$ = [0.64–0.67].
  - o Phase 2: Local scour at the pile: The observed total equilibrium scour depth at the pile contour was S_d = [2.45–2.89 m]; while the

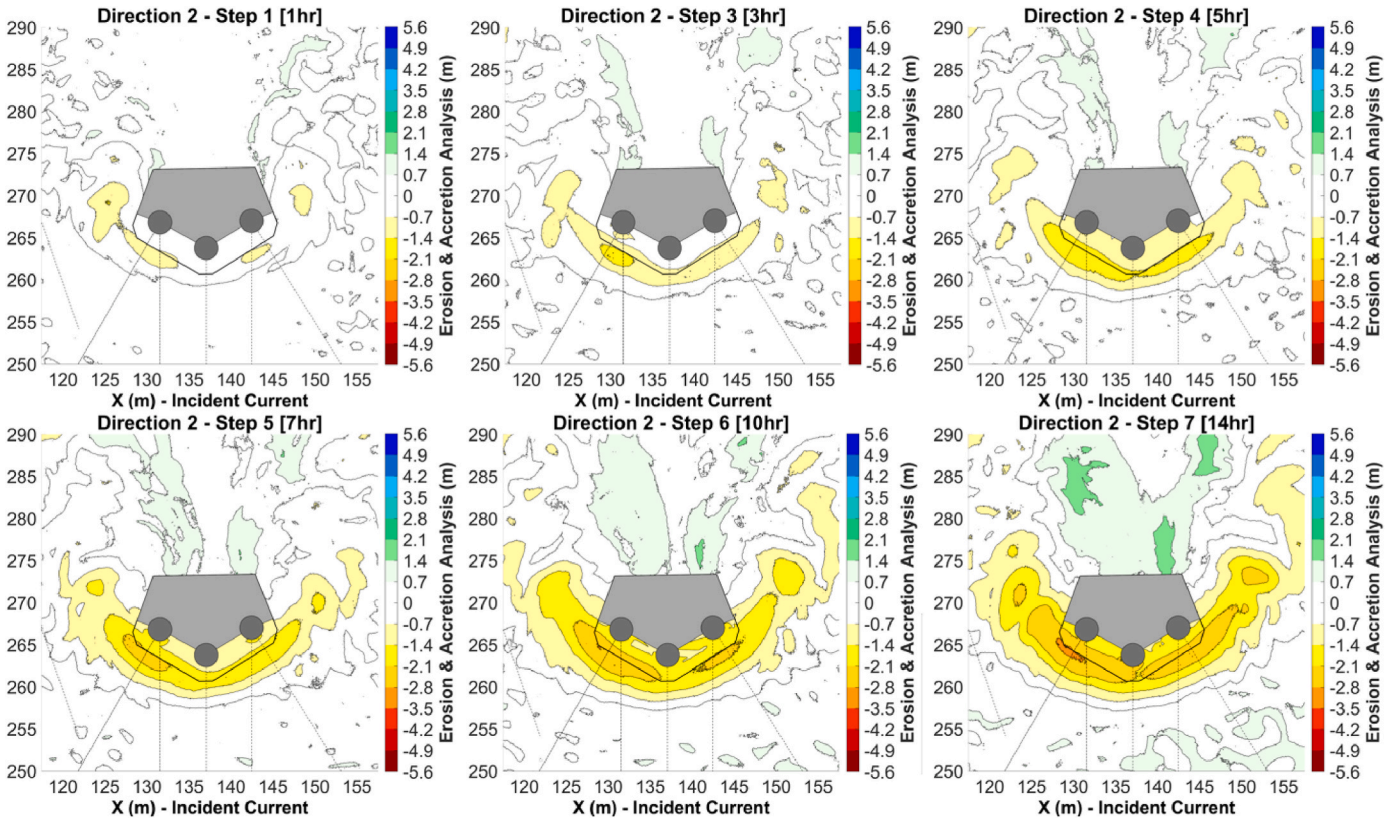

Fig. 17. Orientation #2: Erosion evolution around pile group D2 (time intervals of 2–3–4–5–6–7).

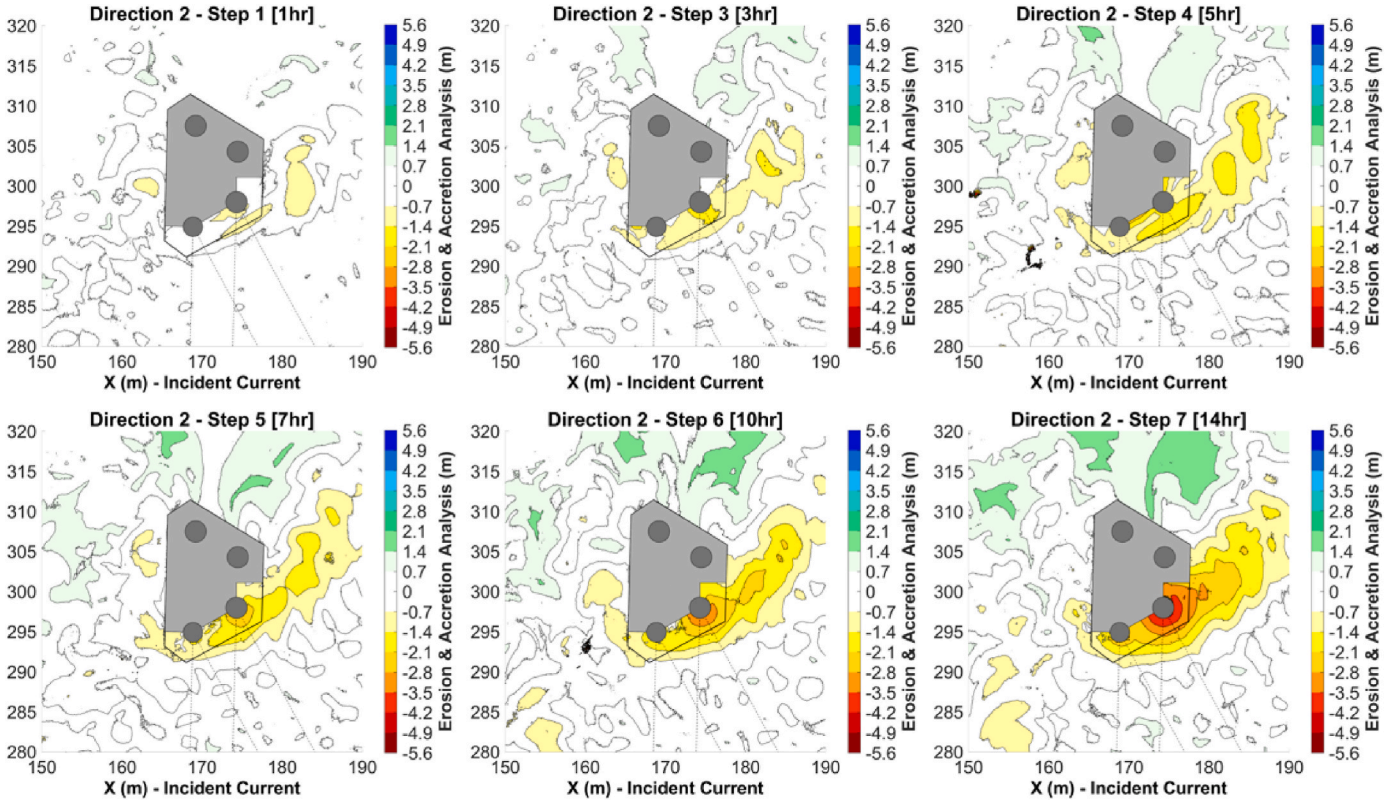

Fig. 18. Orientation #2: Erosion evolution around pile group A1 (time intervals of 2–3–4–5–6–7).

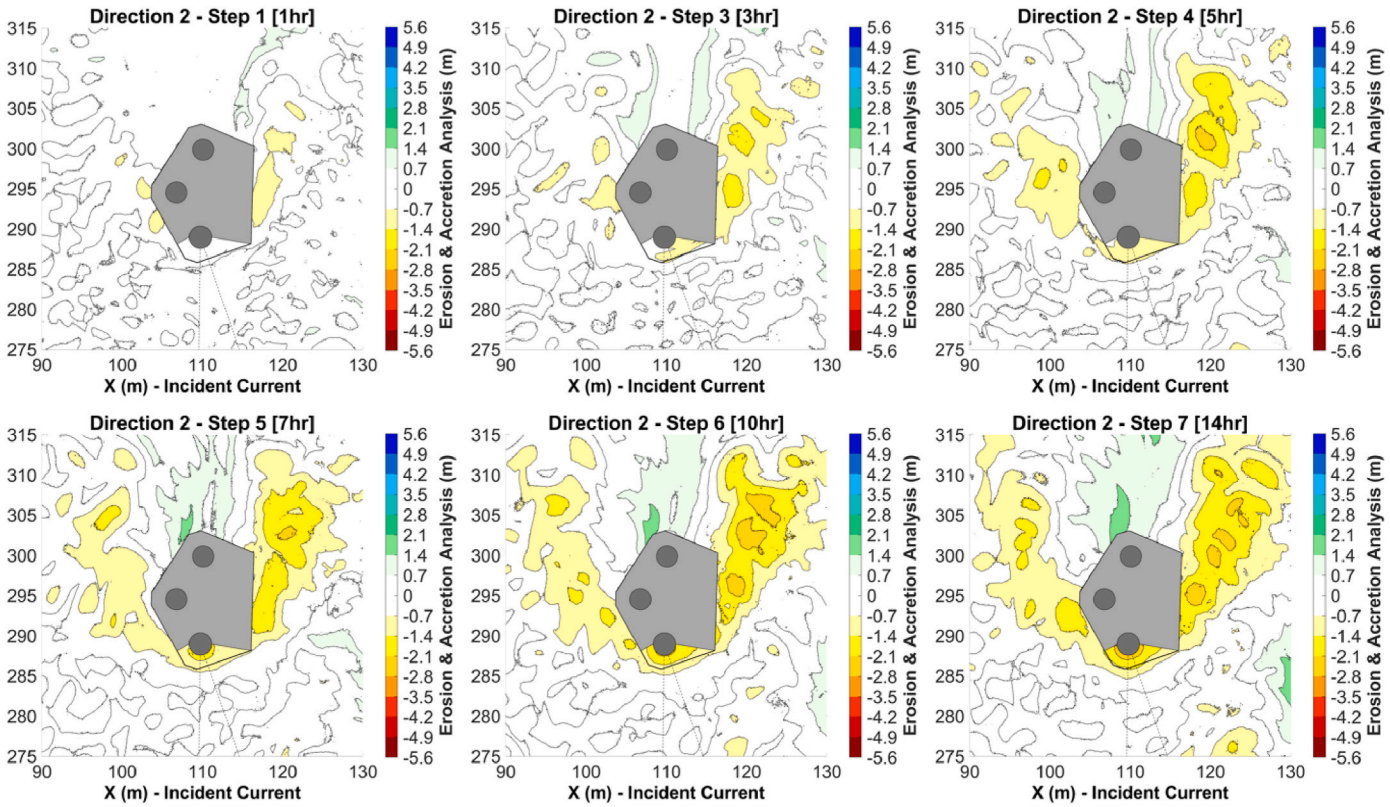

Fig. 19. Orientation2: Pile cluster D1 – Laser scanner measurements (time intervals 2–3–4–5–6–7).

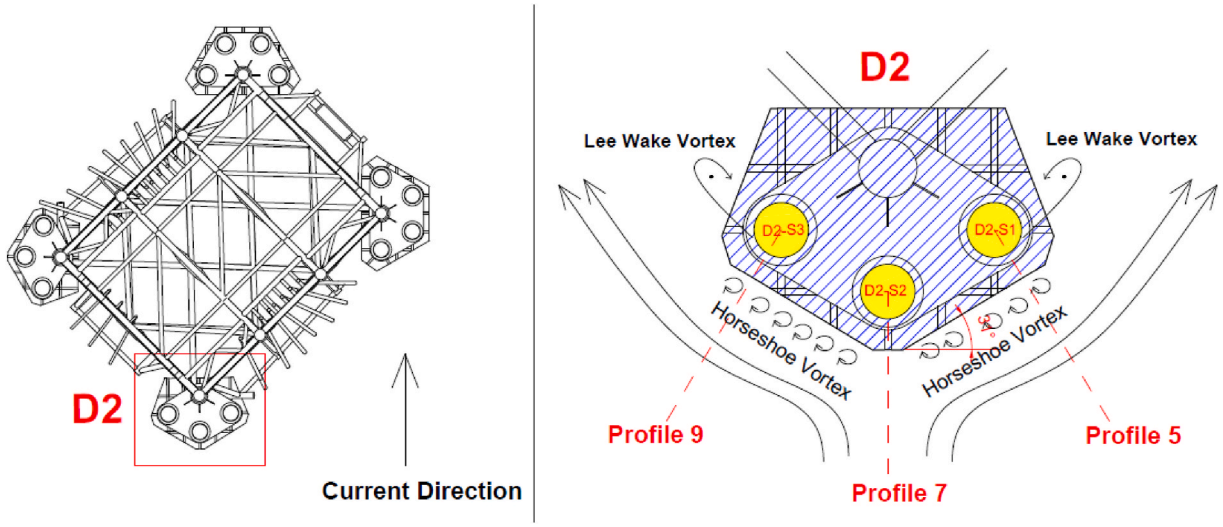

Fig. 20. Orientation #2: Scour around pile cluster D2.

dimensionless scour depth (function of the equivalent diameter) was $\alpha_{Phase\ II} = [1–1.18]$.

- Flow direction 45° with respect to the jacket axes: The most exposed pile clusters were D2, A2 and D1 were directly exposed to the flow.
  - o Pile Cluster D2: The scour Phase number I was only developed on the outer piles D2S1 and D2S3; while in the case of the central pile (D2S2), laser scanner measurements indicated that Phase II (local pile scour) was initiated in the last step of the sequence. Taking into account the previous considerations, only the equilibrium conditions were met in phase I (mud mat contour). The main results for the outer piles are given below:
    - The mud mat contour equilibrium contour depth was S = 2.4–2.7 m.
    - The dimensionless scour depth (a function of the equivalent diameter) was $\alpha_{Phase\ I} = [0.18–0.2]$.
    - The dimensionless scour depth (function of the equivalent diameter and the relative height of the pile cluster) was $\beta_{Phase\ I} = [0.58–0.65]$.
  - o Pile Cluster A2: The maximum scour was observed at pile A2S2. The total equilibrium scour depth at the pile contour observed was $S_d = 5.06$ m. The dimensionless parameters registered were $\alpha = 0.329$ and $\beta = 1.1$. Those values were aligned with the results obtained for the previous direction.

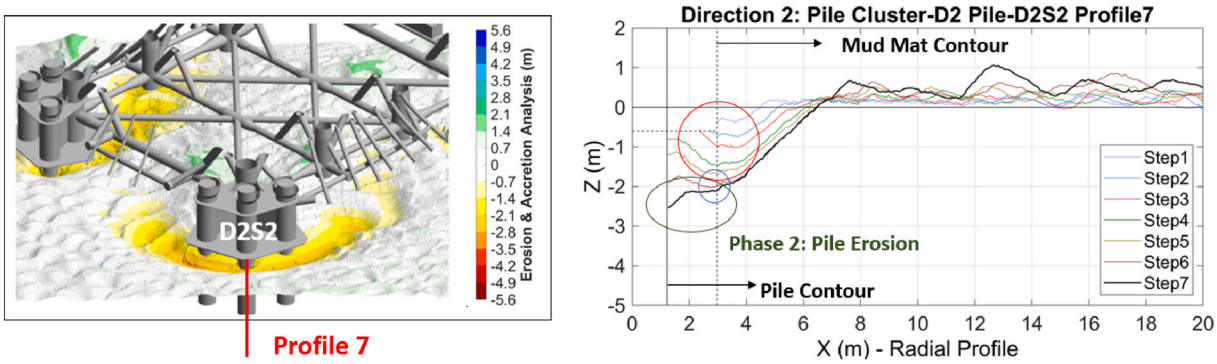

Fig. 21. Orientation #2: PC D2: Longitudinal profile 5 – D2S2.

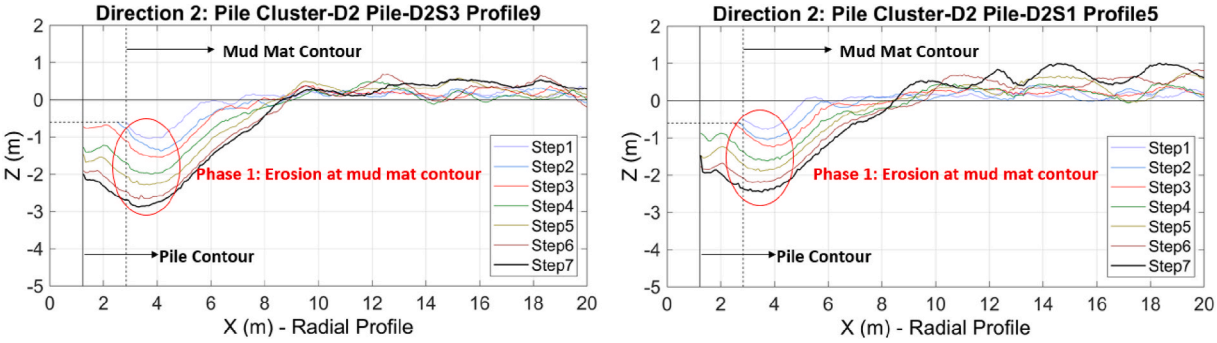

Fig. 22. Equilibrium scour depth on the mud mat contour. Left: in front of pile D2S3 and right: in front of pile D2S1.

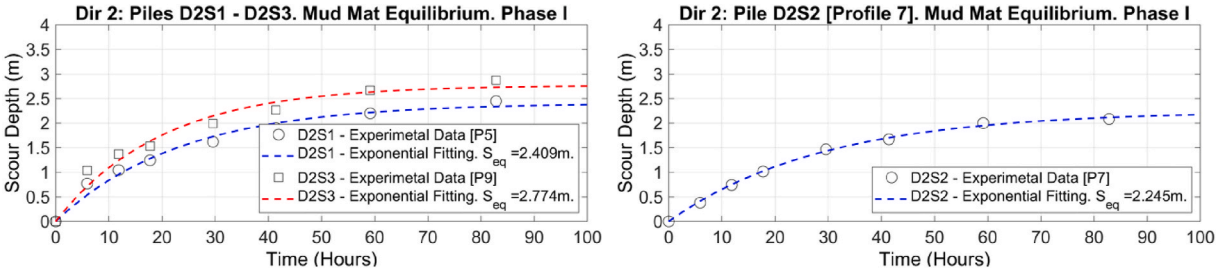

Fig. 23. Orientation #2: Pile cluster D2 – Scour evolution at the mud mat contour: 1) Left: Piles D2S1 (profile 5) and D2S3 (profile 9). 2) Right: Pile D2S2 (profile 7).

Table 9
Orientation #2: Pile cluster D2: Equilibrium scour during phase I (mud mat contour).

Equilibrium Conditions: Phase I			
Pile	Equilibrium Scour Depth (S_{eq})	Dimensionless Scour Depth (1) $\alpha = S_{eq}/D_{eq}$	Dimensionless Scour Depth (2) $\beta = S_{eq}/(D_{eq} x K_h)$
D2S1	2.4	0.18	0.58
D2S2	2.2	0.16	0.53
D2S3	2.7	0.2	0.65

D_{eq} = 13.7 m (equivalent pile diameter)//K_h = 0.299.

- o Pile Cluster D1 The maximum scour was observed at pile D1S3. The total equilibrium scour depth at the pile contour was S_d = 3.5 m. The dimensionless parameters registered were α = 0.38 and β = 1.27. Again, those values were aligned with the results obtained for the previous direction.

The results presented evidence the importance experimental testing when the geometries analysed are complex. The results obtained and the methodology used have improved our understanding of scour mechanisms around complex geometries, the determination of the equilibrium scour depth and the area of influence of the structure. In general terms, the dimensionless scour depth parameters α and β for all pile clusters were consistent.

For similar jacket foundation supported by solid pile clusters, the dimensionless scour depth coefficients proposed can be used as an engineering tool for predicting local scour around solid pile clusters at the early design stages. It is important to notice that the generalization is limited to a certain typology of jackets structures. However, this typology is becoming more popular to ensure the load transmission from the jacket to the ground. In those cases, the semi-empirical approach proposed becomes a useful tool to conduct conceptual studies required by industry.

This novel semi-empirical approach, which is based on the equivalent diameter (D_{eq}) and the pile cluster height (applying the corrector factor K_h), is of significant value for critical structures such as offshore substations, which are traditionally founded on pile clusters. For the most exposed piles, the following equation provides a summary of the upper and lower bounds of the dimensionless total scour depth obtained from the physical tests presented in this paper:

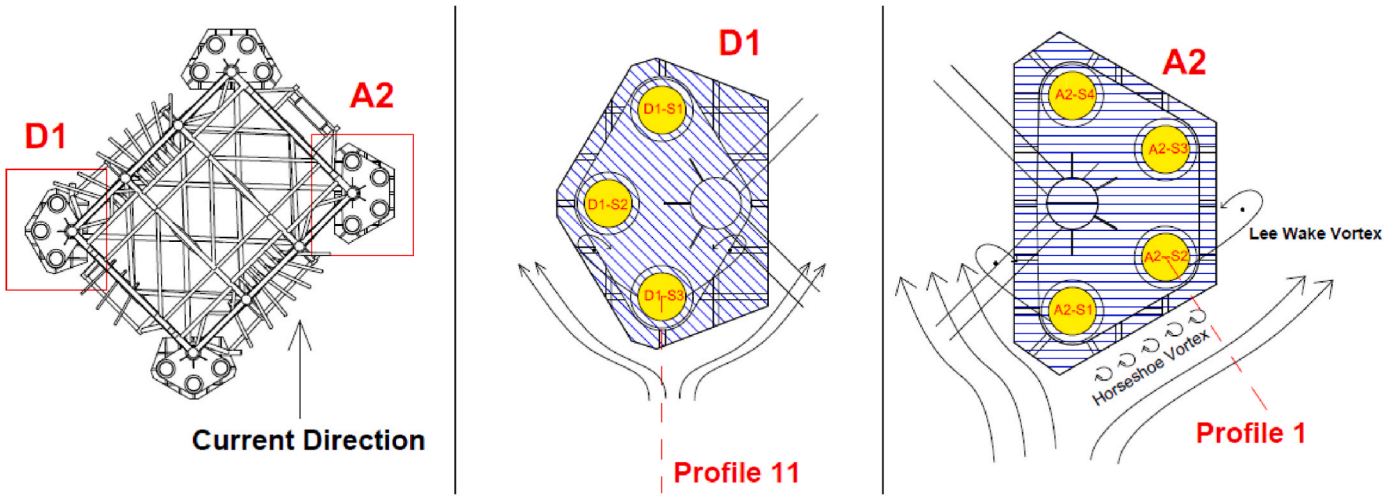

Fig. 24. Orientation #2: Scour around pile clusters D1 and A2.

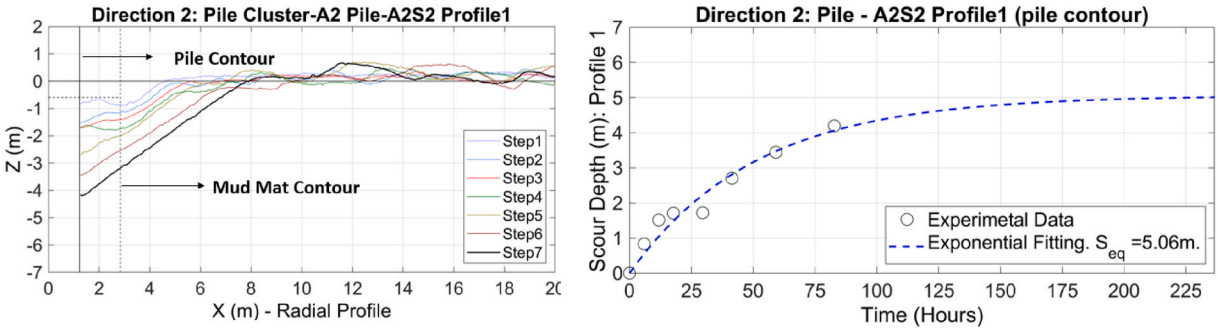

Fig. 25. Orientation #2: Pile A2S2: Left: Longitudinal profiles. Right: Final equilibrium scour at pile A2S2.

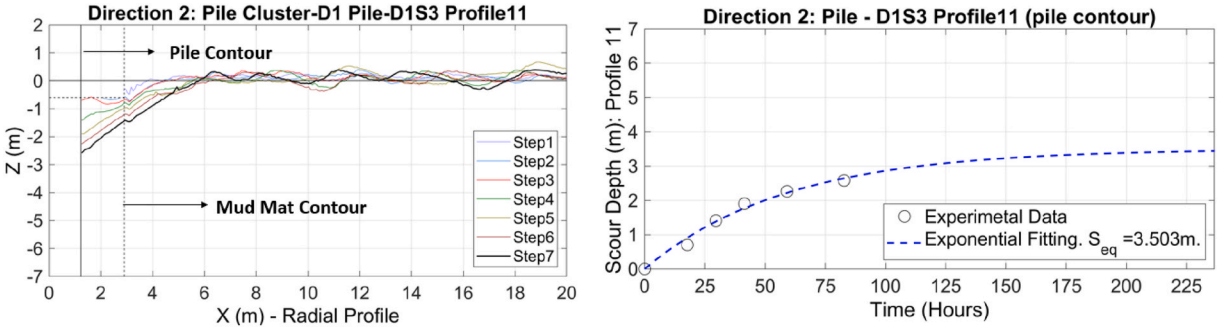

Fig. 26. Orientation #2: Pile D1S3: Left: Longitudinal profiles. Right: Final equilibrium scour at pile D1S3.

$$S_{eq} = \beta^* D_{eq}{}^* K_h, with\ \beta = [1.1 - 1.3] \quad \text{Equation 14}$$

CRediT authorship contribution statement

J. Sarmiento: Writing – original draft, Methodology, Investigation, Formal analysis, Conceptualization. **R. Guanche:** Writing – review & editing, Methodology, Investigation, Funding acquisition, Conceptualization. **I.J. Losada:** Writing – review & editing, Supervision, Investigation, Formal analysis, Conceptualization. **E.M. Rosendo:** Writing – review & editing, Supervision, Funding acquisition. **A. Guindo:** Writing – review & editing, Supervision, Methodology. **J. Ladrón de Guevara:** Writing – review & editing, Supervision, Methodology.

Declaration of competing interest

The authors declare that they have no known competing financial interests or personal relationships that could have appeared to influence the work reported in this paper.

Acknowledgements

The authors would like to thank DRAGADOS OFFSHORE for their support and funding for conducting this research. This study is part of the ThinkInAzul programme and was supported by the Ministerio de Ciencia e Innovación with funding from the European Union NextGeneration EU (PRTR-C17. I1) and Comunidad de Cantabria. This work is also part of the R&D project "Advanced methodology for foundation of

critical structures in offshore wind farms (CREMA)" funded by MCIN/AEI/10.13039/501100011033.

References

Breusers, H.N.C., Nicollet, G., Shen, J., 1977. Local scour around cylindrical piers. J. Hydraul. Res. 15 (3), 211–252.

Chen, H., Zhang, J., Wang, F., Guo, Y., Guan, D., Feng, L., 2023. Experimental investigation of the current induced local scour around a jacket foundation. Ocean Eng. 285, 115369.

Chen, H., Zhang, J., Hou, D., Guo, Y., 2024. On the local scour around a jacket foundation under bidirectional flow loading. Ocean Eng. 310, 118772.

de Sonneville, Ben, Raaijmakers, Tim, Daniel, Rudolph, Rupert, Hunt, Klaas, Rietema, 2011. "Operational Scour Management for Safe Jack-Up Operations," in Proceedings of the ASME 2011 30th International Conference on Ocean, Offshore and Arctic Engineering, vol. 1. Offshore Technology; Polar and Arctic Sciences and Technology, Rotterdam, The Netherlands. June 19–24.

de Sonneville, B., van Velzen, G., Wigaard, J., 2014. Design and optimization of scour protection for offshore wind platform Dolwin Beta. In: Proceedings of the 33rd International Conference on Ocean. Offshore and Arctic Engineering, San Francisco, California, USA.

Den Boon, H., Sutherland, J., Whitehouse, R., Soulsby, R., Stam, C.-J., Verhoeven, K., Høgedal, M., Hald, T., 2004. ". Scour behaviour and scour protection for monopilefoundations of offshore wind turbines,". In: Proceedings of the European WindEnergy Conference, p. 14. *pp (CD-ROM)*.

Evaluating Scour at Bridges, fifth ed., 2012

Gao, Y., Chen, W., Zhou, P., Du, F., Wang, L., 2023. Experimental investigation on scour development and scour protection for offshore converter platform. Mar. Struct. 90, 103440.

Geosystems "https://leica-geosystems.com/products/laser-scanners/scanners/leica-rtc360," [Online].

Hoffmans, G.J.C.M., Verheij, H.J., 1997. Scour Manual. CRC Press, Taylor & Francis Group.

Hu, R., Wang, X., Liu, H., Lu, Y., 2021. Experimental study of local scour around tripod foundation in combined collinear waves-current conditions. J. Mar. Sci. Eng. 9 (12), 1373.

Hughes, S.A., 1993. Physical Models and Laboratory Techniques in Coastal Engineering. World Scientific Publishing Co. Pte. Ltd, Singapore.

Kamphuis, J., 1991. Physical modelling. In: Herbich, J.B. (Ed.), Handbook of Coastal and Ocean Engineering. Gulf Publishing Company, Houston, Texas, Vol2.

Lancaster, O., Cossu, R., Wuppukondur, A., Astorga Moar, A., Hunter, S., Baldock, T.E., 2022. Xperimental measurements of wave-induced scour around a scaled gravity-based Oscillating Water Column Wave Energy Converter. Appl. Ocean Res. 126, 103268.

Larsen, B.E., Fuhrman, D.R., 2023. Re-parameterization of Equilibrium Scour Depths and Time Scales for Monopiles, vol. 185, 104356.

Li, J., Guo, Y., Lian, J., Haijun, W., 2022. Scour effects on the bearing capacity of multi-bucket jacket foundation for offshore wind turbines. Ocean Eng. 259, 111848.

Melville, B., Coleman, S.E., 2000. Bridge Scour. Water Resources Publications,CO.

Offshore Wind in Europe: Key Trends and Statistics 2020, 2020. Wind Europe, Brussels.

Raaijmakers, T., Rudolph, D., 2008. Time-dependent scour development under combined current and waves conditions -laboratory experiments with only monitoring technique. Proceedings 4th Internatinal Conference on Scour and Erosion - ICSE 4 Tokio, Japan, pp. 152–161. November 7-8, 2008.

Raaijmakers, T., Roetert, T., van Steijn, P., 2017. "Scour and Scour Mitigation for Hollandse Kust (Zuid): Recommendations for Foundations and Cables,".

Sarmiento, J., Guanche, R., Iturrioz, A., Ojanguren, T., Ávila, A., Yanes, C., 2021. Experimental evaluation of dynamic rock scour protection in morphodynamic environments for offshore wind jackets. Energies 14 (12), 3379.

Sarmiento, J., Guanche, R., Losada, I.J., Serna, J., 2024a. Experimental analysis of scour around an offshore wind gravity base foundation. Ocean Eng. 308, 118330.

Sarmiento, J., Fernández, S., Guanche, R., 2024b. Methodology to assess scour development around complex structures. J. Phys.: Conf. Series: WindEurope Annual Event 2745, 012020.

Sheppard, M., Asce, M., Miller Jr., W., 2006. Live-Bed local pier scour experiments. J. Hydraul. Eng. 635–642.

Shields, A., 1936. Anwendung der Aehnlichkeitsmechanik und der Turbulenzforschung auf die Geschiebebewegung. Mitt. Preuss. Versuchsanst. Wasserbau Schiffbau 26, 36.

Soulsby, R., 1997. Dynamics of Marine Sands: A Manual for Practical Applications. Thomas Telford, London.

Sumer, B.M., Fredsøe, J., 2002. The mechanics of scour in the marine environment. World Sci. https://doi.org/10.1142/4942. ISBN: 981-024930-6.

Sumer, B.M., Christiansen, N., Fredsøe, J., 1992a. Time scale of scour around a vertical pile. In: The Second International Offshore and Polar Engineering Conference. *14-19 June, San Francisco, California, USA*.

Sumer, B.M., Fredsøe, J., Christiansen, N., 1992b. Scour around vertical pile in wave. J. Waterw. Port, Coast. Ocean Eng. 118 (1), 15–31.

Smulders. https://www.smulders.com/pl/iemants-and-jan-de-nul-to-build-gravity-based-foundations-for-kriegers-flak. (Accessed 8 May 2023) [Online].

Veldhuizen, R., Broekema, Y., Bruinsma, N., 2023. Scour Development in layered soils around offshore monopile foundations. In: Proceeding of the 11th International Conference on Scour and Erosion. Copenhagen, Denmark.

Welzel, M., Schendel, A., Satari, R., Neuweiler, I., Schlurmann, T., 2024. Spatio-temporal analysis of scour around complex offshore foundations under clear water and live bed conditions. Ocean Eng. 298, 117042.

Welzen, M., Schendel, A., Hildebrandt and, A., Schlurmann, T., 2019. Scour development around a jacket structure in combined waves and current conditions compared to monopile foundations. Coast Eng. 152, 103515.

Whitehouse, R., 1998. Scour at Marine Structures: A Manual for Practical Applications. Thomas Telford Limited.

Whitehouse, R.J.S., 2006. Scour at Coastal Structures (Invited Lecture). Gouda, The Netherlands.

Whitehouse, R.J., Stroescu, E.I., 2023. Scour depth development at piles of different height under the action of cyclic (tidal) flow. Coast Eng. 179, 104225.

Whitehouse, R., Harris, J.M., Mundon, T., Sutherland, J., 2010. Scour at offshore structures. In: Proceedings of the Fifth International Conference on Scour and Erosion (ICSE-5). San Francisco, California.

Wind Energy in Europe: 2023 Statistics and the Outlook for 2024-2030, 2024. Brussels.

Yang, Y., Qi, M., Wang, X., Li, J., 2020. Experimental study of scour around pile groups in steady flows. Ocean Eng. 195, 106651.

Yuan, C., Melville, B.W., Adams, K.N., 2017. Scour at wind turbine tripod foundation under steady flow. Ocean Eng. 141, 277–282.

Zhang, J., Chen, H., Guo, Y., Wang, F., Guan, D., Deng, X., Hou, D., 2024. Experimental study on the scour characteristics around a jacket foundation under wave actions. Ocean Eng. 299, 117290.